Along-strike coupling heterogeneity in Cascadia's slow-slip zone constrained by GNSS and reduced-order rate-and-state friction modeling

Yohai Magen, Alice-Agnes Gabriel, Dave A. May

This manuscript has been submitted for publication in *Geophysical Research Letters*. This version is a non-peer-reviewed preprint submitted to *EarthArXiv*.

Please note that the manuscript has yet to be formally accepted for publication. Subsequent versions of this manuscript may have slightly different content.

March 6, 2026

Along-strike coupling heterogeneity in Cascadia's slow-slip zone constrained by GNSS and reduced-order rate-and-state friction modeling

Yohai Magen[1], Alice-Agnes Gabriel[1,2], Dave A. May[1]

[1]Institute of Geophysics and Planetary Physics, Scripps Institution of Oceanography, University of California San Diego, La Jolla, CA 92093, USA
[2]Department of Earth and Environmental Sciences, Ludwig-Maximilians-Universit, 80333, Munich, Germany

Key Points:

- Inter-SSE coupling in the Cascadia ETS zone varies along strike, from ∼0.6 in the north to ∼0.5 in central Cascadia and ∼0.35 in the south.
- ROM-accelerated rate-and-state friction simulations show that effective normal stress controls SSE recurrence; coupling controls SSE moment.
- Coupling from GNSS inversion and physics-based Bayesian inference indicate incomplete inter-SSE slip-deficit release in central Cascadia.

Corresponding author: Yohai Magen, ymagen@ucsd.edu

Abstract
Slow slip events (SSEs) in the Cascadia subduction zone exhibit along-strike segmentation, where the central segment has longer recurrence intervals but smaller moments. We quantify the controls on this variability by combining geodetic inter-SSE coupling inversion with Bayesian inference of a quasi-dynamic rate-and-state friction SSE-cycle model accelerated by reduced-order modeling. We find that effective normal stress primarily controls SSE recurrence interval, whereas inter-SSE coupling heterogeneity governs along-strike moment variability. Our independent inversion of inter-SSE GNSS velocities yields mean coupling of ∼60% in northern Cascadia, ∼48% in central Cascadia, and ∼34% in southern Cascadia, with lower long-term coupling. Comparing inter-SSE and long-term coupling suggests that transient SSEs recover ∼1/3 of the slip deficit in the north and south but only ∼16% in central Cascadia, implying persistent slip-deficit accumulation in the central margin. Together, these results suggest that coupling heterogeneity provides a unified geodetic and physics-based explanation for Cascadia SSE segmentation.

Plain Language Summary

The Cascadia subduction zone, which stretches from northern California to Vancouver Island, is a major hazard capable of producing large, damaging earthquakes and tsunamis. In addition to these rare, large events, the megathrust also experiences "slow-slip events" deep underground, repeating every 8 to 20 months. These events release energy slowly over days or weeks rather than seconds and are too slow to be felt by humans, though they are detected by GPS stations on the surface. In this study, we combine GPS data with computer simulations and machine learning to understand why these slow-slip events vary in frequency and size along the coast. We find that how strongly the two sides of the subduction interface are stuck together varies from north to south. Northern Cascadia is stuck more tightly together between slow-slip events than the central and southern sections. Our models suggest that slow slip events do not release all accumulated strain in the central section, which might need to be released in the future, whether in a slow-slip event or as part of a large megathrust earthquake. This helps us better understand how strain builds up along the subduction zone, which is critical for assessing regional long-term earthquake hazard.

1 Introduction

Slow slip events (SSEs) are transient slip events, spanning days to months, that can occur up-dip or down-dip of the seismogenic portion of global megathrusts (Bürgmann, 2018; Dascher-Cousineau & Bürgmann, 2024). Such slow transient slip is often accompanied by a low-amplitude, extended-duration (minutes to days) seismic signal named tectonic (non-volcanic) tremor, and the combined phenomenon is termed Episodic Tremor and Slip (ETS, Rogers & Dragert, 2003; Brown et al., 2009). ETS are part of a broad spectrum of possible mechanisms to relieve stress accumulated on subduction zone interfaces from fast, potentially devastating earthquakes to continuous creep (Ide & Beroza, 2023; Peng & Gomberg, 2010). Over the past 25 years, SSEs have been well-documented phenomena in the Cascadia subduction zone (CSZ) in the Pacific Northwest (Dragert et al., 2001), yet the mechanisms driving their spatio-temporal kinematics are not fully understood (Behr & Bürgmann, 2021; Gomberg et al., 2016). Understanding how much tectonic loading is released during those SSEs and how much is accumulated on the ETS zone is essential for understanding the subduction zone's long-term stress accumulation and mitigating seismic and tsunami hazards.

The CSZ is formed by the young and hot Juan de Fuca plate to the north and the Gorda microplate to the south, which are subducting in an eastward motion beneath the North American plate at a rate of ∼3.7 cm/year (DeMets et al., 2010, Figure 1a). The margin exhibits along-strike segmentation in past earthquake slip, state of kinematic cou-

pling, and distribution of ETSs (e.g., Audet & Bürgmann, 2014; Brudzinski & Allen, 2007; Morton et al., 2023; Schmalzle et al., 2014; Wang et al., 2013; Watt & Brothers, 2020; Carbotte et al., 2024; Goldfinger et al., 2025). The reasons underlying this segmentation are challenging to constrain, partly due to the rapid decrease in geodetic resolution with distance from the coast (Lindsey et al., 2021). In addition, the interplay of variations in structural and frictional properties, kinematic geodetic coupling and prestress, remain poorly understood (Watt & Brothers, 2020; Walton et al., 2021; Carbotte et al., 2024). The relative abundance of slow slip observations and their spatial location within a relatively short distance from the geodetic network provide an opportunity to understand the sources of the CSZ's along-strike segmentation and the underlying driving factors.

Numerical simulations leveraging rate-and-state friction laws have reproduced key aspects of Cascadia's slow slip cycle, including observed recurrence intervals (Liu & Rice, 2009), sensitivity to slab geometry (Li & Liu, 2016), fluid interaction (Segall et al., 2010; Ozawa et al., 2025), and along-strike segmentation (Li & Liu, 2017). However, the link between frictional properties, kinematic coupling, and segmentation remains incompletely resolved.

ETS observations partition the CSZ into northern, central, and southern segments based on variation in SSE recurrence interval, slip magnitude, and tremor density (Figure 1, Brudzinski & Allen, 2007; Audet & Bürgmann, 2014; Bartlow, 2020; Gualandi, 2025; Zhang & Houston, 2025). Offshore of Vancouver Island and Washington state in northern Cascadia, SSEs are larger ($\sim M_w6.6$) with a regular recurrence interval of 14 ± 2 months. Central Cascadia, offshore of Oregon state, experiences longer recurrence intervals of 19 ± 4 months and counterintuitively shows smaller magnitude ($\sim M_w6.45$) than its northern counterparts although it is ∼100 km longer along-trench (see, e.g., Fig. S8). To the south, where the CSZ approaches the complex Mendocino triple junction with the San Andreas and Mendocino strike-slip faults to the south and west, respectively, ETS activity shows a shorter recurrence interval of 10 ± 2 months (Brudzinski & Allen, 2007) and small magnitude SSEs ($\sim M_w6.0$, Michel et al., 2019) with complex temp-spatial distribution (Nuyen & Schmidt, 2024).

Here, we investigate the mechanical properties driving the along-strike segmentation of the CSZ. We derive the inter-SSE Global Navigation Satellite System (GNSS) velocity field following the method of Bartlow (2020) and invert for the subduction coupling within the ETS zone. The inversion shows a mean coupling of ∼60% in northern CSZ, ∼48% in central Cascadia and ∼34% in the southern segment. To understand the physical implications of this heterogeneity, we use Bayesian inversion of a 2D rate-and-state friction model (Dieterich, 1979; Ruina, 1983), accelerated by scientific machine-learning reduced-order modeling (Magen, May, & Gabriel, 2026). We specifically analyze if variations in megathrust coupling and effective normal stress can explain the diverse SSE moment and recurrence interval observed along strike. By integrating geodetic coupling inversion and physics-based modeling, we demonstrate that along-strike variation in megathrust locking and elevated fluid pore-fluid pressure are required to explain CSZ ETS segmentation.

2 GNSS Data Processing and Geodetic Coupling Inversion

We derive the inter-SSE velocity field in the Pacific Northwest from the daily time series of 446 GNSS stations processed by the Nevada Geodetic Laboratory (NGL, Blewitt et al., 2018) in a fixed North America reference frame (Text S1). To resolve the distinct components of the ETS cycle, we decompose each station time series into inter-SSE velocities, the assumed steady motion between SSEs, SSEs transient offsets, and a seasonal signal, following the methodology of Bartlow (2020). To identify and mask transient SSE deformation, we use periods of high tremor productivity from the CSZ regional

catalog (Wech & Creager, 2008; Wech, 2010, 2021). While we remove coseismic offsets, inter-SSE velocities near the Mendocino Triple Junction may be influenced by residual post-seismic deformation from multiple $M_w \geq 6.0$ earthquakes, including the 2021 M_w6.1 and M_w6.0 Petrolia, 2022 M_w6.4 Ferndale, and 2024 M_w7.0 Mendocino earthquakes, reflecting the modeling challenges inherent to this complex triple junction. This GNSS processing chain yields a velocity field representing the steady deformation during the periods between SSEs, excluding the transient deformation contribution (Figure 1).

We invert our derived inter-SSE velocity field and long-term velocity field (MIDAS, Blewitt et al., 2018) to determine the inter-SSE and long-term coupling distribution across the megathrust, using Slab2 geometry (Hayes et al., 2018). We determine the spatially variable coupling coefficient ($\boldsymbol{c}$) by minimizing the regularized least-squares misfit (see Text S2):

$$\underset{\boldsymbol{c},\boldsymbol{\theta}}{\operatorname{argmin}} \left(\|\boldsymbol{A}\boldsymbol{m}(\boldsymbol{c},\boldsymbol{\theta}) - \boldsymbol{d}\|_2^2 + \beta \|\boldsymbol{D}\boldsymbol{m}(\boldsymbol{c},\boldsymbol{\theta})\|_2^2 \right) \quad \text{s.t.} \quad 0 \leq c_i \leq 1, \tag{1}$$

where $\boldsymbol{A}$ are the elastic Green's functions (Okada, 1992; Nikkhoo & Walter, 2015), $\boldsymbol{d}$ is the observed surface velocity field, and $\boldsymbol{m}(\boldsymbol{c},\boldsymbol{\theta})$ is the predicted surface velocity due to megathrust back-slip (Savage, 1983). The back-slip rate is parameterized by the coupling vector ($\boldsymbol{c}$), where c_i denotes the coupling coefficient of the i^{th} megathrust patch, the rake vector ($\boldsymbol{\theta}$), and a long-term convergence rate of 3.7 cm/year (DeMets et al., 2010). The discrete gradient matrix $\boldsymbol{D}$ is applied to the megathrust back-slip rate, and β is the smoothing coefficient that controls the strength of regularization.

Geodetic resolution decreases rapidly with distance from onshore-only observational network (Lindsey et al., 2021). To mitigate limited offshore resolution, previous studies typically impose additional assumptions on coupling distribution (Schmalzle et al., 2014; Lindsey et al., 2021; Saux et al., 2022). Here, we focus on coupling in the ETS region, which we define as the set of $0.05° \times 0.05°$ grid cells with more than 75 identified tremors (Wech & Creager, 2008; Wech, 2010, 2021). This ETS region lies at 25-50 km depth and ∼10 km inland. It is a portion of the subduction interface that is relatively close to the geodetic network and therefore better resolved than the shallower portions.

To evaluate the reliability of our inversion within the ETS zone, we analyze the model resolution and model covariance (Figure S4). The resolution matrix identifies which model parameters are uniquely resolved by the data. The model covariance matrix maps the GNSS data uncertainties in the inferred model parameters. Together, this analysis enables us to evaluate whether the onshore geodetic network can robustly resolve coupling variations within the ETS region.

3 Monte Carlo Markov Chain Bayesian inference using reduced-order modeling

We use a Monte Carlo Markov Chain (MCMC, Hastings, 1970) approach to infer the posterior probability distribution of three parameters governing the SSEs characteristics: the ETS-zone width (W), effective normal stress (σ_W), and the mean coupling in the ETS zone ($\hat{c}$). The inversion is constrained by observed SSE recurrence intervals (T_c^{obs}) and moments (M_0^{obs}) from the geodetic inversion of Michel et al. (2019), which are consistent with tremor-based recurrence time estimates (Brudzinski & Allen, 2007, Table S1 and Figure S8).

The forward models are 2D quasi-dynamic SSE cycle simulations in a Cascadia-like subduction zone setting (Figure 2, Magen, May, & Gabriel, 2026). Megathrust friction follows rate-and-state friction, and the state variable evolves according to the ageing law (Dieterich, 1979; Ruina, 1983, see Text S3). We generate a data set of 110 simulations using the open source software `Tandem` (Uphoff et al., 2022; Gabriel et al., 2025),

varying $W \in [62.5, 100]$ km and $\sigma_W \in [1, 10]$ MPa to explore the parameter space controlling Cascadia's along-strike segmentation. This expands the range of $\sigma_W \in [1, 6]$ MPa explored in Magen, May, and Gabriel (2026) which focused on northern Cascadia.

Evaluating all required forward models within the MCMC inversion is, however, computationally infeasible, because convergence to the posterior distribution typically requires $\mathcal{O}(10^4)$–$\mathcal{O}(10^5)$ model evaluations (Mosegaard & Tarantola, 1995; Cui et al., 2015). To accelerate the Bayesian inference, we replace the full-order numerical simulations with a reduced-order model (ROM, Sirovich, 1987; Benner et al., 2015) that serves as a non-intrusive data-driven surrogate ROM approaches have been recently applied to a range of computational Geophysics applications such as, seismic shake maps (Rekoske et al., 2023), wave fields (Rekoske et al., 2025), thermal structure in subduction zones (Hobson & May, 2025), geothermal geodynamic processes (Degen et al., 2023), and slow slip sequences (Kaveh et al., 2024; Magen, May, & Gabriel, 2026).

Our specific ROM methodology follows Magen, May, and Gabriel (2026) and is a two-stage approach that comprises a computationally intensive ROM construction stage performed only once and dominated by the cost of the forward models, and an inference stage in which we evaluate unseen models in a fraction of the computational cost (Text S4. Evaluating $ROM(W^*, \sigma_W^*)$ takes only ∼30 seconds on a single CPU, corresponding to a speedup of $\mathcal{O}(10^5)$ compared to the typical ∼2,000 CPU hours required to run a single `Tandem` simulation.

In the MCMC, we assume uniform prior distributions for $\sigma_W \in [1, 10]$ MPa, and $\hat{c} \in [0, 1]$. For W (in km), we assume a normal distribution which parameters are derived from the local width of the ETS area (Text S5, Figure S11).The posterior distribution is sampled using the Metropolis-Hastings algorithm (Hastings, 1970). For each proposed parameter vector $(W^*, \sigma_W^*, \hat{c}^*)$, we evaluate $ROM(W, \sigma_W)$ to obtain the predicted recurrence interval T_c^{ROM} and a characteristic moment M_0^{ROM} (Text S5). This moment is calculated by extruding the 2D model-predicted SSE slip along-strike (Liu & Rice, 2009). The 3D extrapolation is motivated by the high aspect ratio characteristic of large Cascadia SSEs, for which the along-strike slip length (hundreds of kilometers) far exceeds the down-dip width W (∼60-70 km) (Gualandi, 2025). Because the such inferred moment does not match the observed characteristic moments (Fig. 2c,d), we scale it by a model-wide defined empirical factor, $\hat{c}$. The likelihood function $\mathcal{L}((T_c^{obs}, M_0^{obs})|(W^*, \sigma_W^*, \hat{c}^*))$ is given by:

$$\mathcal{L}((T_c^{obs}, M_0^{obs})|(W^*, \sigma_W^*, \hat{c}^*)) \propto \exp\left[-\frac{1}{2}\left(\frac{(T_c^{obs} - T_c^{ROM})^2}{\sigma_{T_c}^2} + \frac{(M_0^{obs} - \hat{c}M_0^{ROM})^2}{\sigma_{M_0}^2}\right)\right] \quad (2)$$

4 Results

4.1 Along-strike segmentation of ETS-zone coupling from GNSS

Our inversion of the inter-SSE and long-term GNSS velocity fields reveals along-strike segmentation in the locking state of the Cascadia ETS zone. The derived inter-SSE velocity field shows velocity magnitudes that are on average ∼10% higher than the long-term GNSS velocities (Blewitt et al., 2018) over the 446 GNSS stations used in this study (Figure 4). The Northern Cascadia SSE region has a mean coupling of ∼60% during the inter-SSE period, with a maximum coupling of 77% and a long-term coupling of ∼26%. The border between Northern and central Cascadia is strongly coupled in the inter-SSE period, with the peak coupling values of the northern segment occurring at the segment border. South of this strongly coupled boundary, the central segment shows a maximum coupling of 63%, with mean values over the entire segment of ∼48% and ∼32% for the inter-SSE and long-term periods, respectively. The boundary between the central and southern segments is completely decoupled at both inter-SSE and long-term timescales, suggesting constant creep at the SSE depth. The Southern Cascadia segment shows the

weakest coupling, with ∼34% coupling during the inter-SSE period and being almost completely decoupled in the long term.

The difference between the inter-SSE and long-term coupling quantifies the fraction of megathrust slip deficit recovered by transient slow slip (Michel et al., 2025).

We emphasize that such geodetically inferred kinematic coupling is an effective, spatially smoothed estimate (e.g., GNSS resolution, assumed geometry, and spatial regularization) and is therefore only approximately comparable to the segment-averaged coupling parameter $\hat{c}$ introduced in our 2-D ROM–MCMC framework (Sec. 3). Although the long-term mean coupling differs between northern and southern Cascadia, transient SSEs are responsible for ∼35% of the recovered slip in both of these regions. In contrast, transient SSEs account for only ∼16% of the recovered slip in central Cascadia, suggesting that ∼32% of the interseismic slip is accumulated as slip deficit at SSE depths in Central Cascadia.

4.2 ROM exploration of physics-based SSE-cycle models

We use our ROM-accelerated SSE-cycle modeling framework (Sec. 3) to connect the geodetically inferred along-strike segmentation of ETS coupling (previous subsection) with constraints on frictional model parameters and SSE source properties. Our ROM approach enables a comprehensive exploration of the modeled SSE recurrence intervals and moments over the (W, σ_W) parametric plane for which we use 15,000 ROM evaluations complementing the 110 forward simulations.

Consistent with previous findings for northern Cascadia (Liu & Rice, 2007; Li & Liu, 2016; Magen, May, & Gabriel, 2026), we find that the magnitude of the effective normal stress acts as the primary control of the SSE recurrence interval across the entire margin (Figure 2a). Varying σ_W from 1 to 10 MPa reproduces the full range of recurrence intervals observed across all three Cascadia segments. However, a discrepancy emerges when modeling SSE moments (Figure 2). In our 2D SSE-cycle model framework, no combination of parameters can simultaneously reproduce both the observed SSE recurrence interval and characteristic moment for southern and central Cascadia. Only in northern Cascadia do the observed recurrence and moment contours intersect within the physical parameter space (blue contours in Figure 2c,d). This suggests that the 2D numerical simulations systematically overestimate moment release relative to geodetic estimates.

To reconcile the SSE cycle models with geodetic observations (Michel et al., 2019), we invert the observed characteristic SSE moments and recurrence intervals for three parameters: the effective normal stress (σ_W) in the SSE source region, the width of the ETS zone (W), and an empirical scaling term ($\hat{c}$). We interpret $\hat{c}$ as the mean coupling (c) over the ETS zone, scaling the simulation's moment. $\hat{c}$ is useful as a posteriori to bridge between the SSE simulations and the geodetic inferences. The 2D rate-and-state friction model predicts inter-SSE slip rates of $\sim 10^{-12}$ m/s, implying coupling close to 100%, in contradiction to the $\sim 40 - 60\%$ derived geodetically.

4.3 ROM-accelerated Bayesian inversion and posterior constraints

We perform a ROM-accelerated physics-based MCMC inversion to identify the ETS-zone width, effective normal stress, and an empirical coupling scaling factor ($\hat{c}$) required to reproduce the diverse SSE characteristics observed along the Cascadia margin. To evaluate the information gained from the inversion, we apply the two-sample Kolmogorov-Smirnov test (Jr., 1951). The test confirms that posterior distributions of the ETS-zone width are statistically different from the tremor-based prior distribution we derived from the spatial distribution of tectonic tremors in all three segments (Text S5). However, the posterior means and uncertainties remain close to the assumed priors, with inferred widths

of 69.4±3.3 km, 64.0±1.0 km, and 67.6±3.5 km for the northern, central, and southern segments, respectively (Figure 3b).

For effective normal stress amplitude and coupling scaling factor, the posterior distributions are clearly different from the uniform priors. Effective normal stress is primarily constrained by the observed recurrence intervals, where values of 4.0±1.1 MPa, 6.1± 2.2 MPa, and 2.7 ± 1.0 MPa (Figure 3a) correspond to recurrence intervals of $13.52 \pm$ 1.4 months, 20.5±3.7 months, and 7.0±4.0 months on the northern, central, and southern segments, respectively. To reconcile the seismic moments, the inversion requires mean inter-SSE coupling coefficients of 0.64±0.24 in the north, 0.45±0.25 in the central segment, and 0.38 ± 0.24 in the south (Figure 3c), consistent with the independently derived geodetic kinematic coupling. This agreement suggests that spatial variations in inter-SSE coupling are an important mechanism regulating the along-strike segmentation of Cascadia's slow slip events. Together, these results support a link between along-strike variations in inter-SSE coupling and the segmentation of Cascadia slow slip.

5 Discussion

Our results demonstrate that spatially distinct regimes of effective normal stress and inter-SSE megathrust coupling primarily control the along-strike segmentation of recurrence intervals and seismic moments segmentation of Cascadia's SSEs. We suggest that the different recurrence intervals observed in the three Cascadia segments are due to variations in effective normal stress, ranging from 2.7 to 6.1 MPa. This low effective normal stress is consistent with V_p/V_s velocity measurements (Audet & Bürgmann, 2014). Previous numerical results for the Cascadia and other subduction zones also suggest that deep SSEs occur under near-lithostatic pore fluid pressure conditions (Liu & Rice, 2009; Perez-Silva et al., 2023; Rubin, 2008; Ozawa et al., 2025). In Cascadia, our results imply pore-fluid pressures of ∼99.3% to 99.7% of lithostatic stress assuming a uniform crust density of 2670 kg/m^3, and that these slight variations can account for most of the observed variation in recurrence intervals.

In contrast to SSE recurrence intervals, our numerical models indicate that SSE moment is controlled primarily by inter-SSE coupling. The inferred variations in ETS-zone width are too small to explain the observed differences in the characteristic moments. For example, the Northern Cascadia ETS zone is only ∼10% wider than in Central Cascadia, based on numerical simulations and observed tectonic tremor productivity, which cannot explain the 60% difference in SSE moments.

If the ETS zone were fully coupled ($c = 1$), the accumulated moment deficit would far exceed the moment release observed in periodic SSEs (Michel et al., 2019). On the other hand, the inter-SSE coupling value must be larger than 0 to produce SSEs. This suggests the ETS zone is partially looked, as we here infer geodetically. To reconcile the numerical simulation with this observation we introduce the a posteriori scaling parameter $\hat{c}$. We hypothesize that $\hat{c}$ can represent 3D heterogeneity (Carbotte et al., 2024; Luo & Liu, 2021), along-strike variations in frictional properties (Brudzinski & Allen, 2007; Luo & Ampuero, 2018), fluid-related processes (Segall et al., 2010; Perez-Silva et al., 2023; Ozawa et al., 2025), or thermal processes (Behr & Bürgmann, 2021; Bürgmann, 2018) not captured in our 2D SSE-cycle model. These process could effectively reduce the inferred coupling parameter. While $\hat{c}$ is an empirical parameter, it serves as a useful first-order approximation and motivates the subsequent ROM–MCMC inversion for$(W, \sigma_W, \hat{c})$. Our inferred inter-SSE coupling, which we derive from numerical and geodetic modeling, suggests that SSEs relieve all or almost all of the slip deficit accumulated in the Northern and Southern Cascadia segments. In central Cascadia, ∼40% of the plate convergence rate is accumulated as a slip deficit in the ETS zone. This may suggest two possible scenarios: the slip deficit may be accommodated during a future Cascadia megathrust earth-

quake, or it may be relieved by long-term variation in SSE recurrence intervals (Luo & Liu, 2019).

We caution that the onshore-only geodetic network and the spatial regularization in our kinematic inversion necessarily smooths potential coupling heterogeneity along the ETS zone (Figure S5). Moreover, our 2D quasi-dynamic SSE cycle simulations, and consequently the ROM surrogate, rely on prescribed geometry and frictional constitutive law choices which may neglect unresolved 3D heterogeneity or coupled hydrologic/rheologic processes. Thus, we interpret the inferred coupling and effective normal stress parameters as segment-scale, effective values.

Finally, inter-SSE coupling might also control the along-strike propagation of SSEs between segments. Gualandi (2025) shows that SSEs can sometimes slip across the Northern and Central segments during a single SSE, whereas no SSEs rupture across the Central-Southern segment boundary. Consistent with this asymmetry, our geodetic coupling inversion finds a highly coupled boundary between the northern and Central Cascadia segment. In contrast, the boundary between the central and southern segments is constantly creeping. In addition, Carbotte et al. (2024) identified major strike-slip faults in the subducting Gorda-Juan de Fuca plates, using detailed seismic imaging, which bound crustal blocks. These lower plate faults spatially coincide with the segmentation boundaries identified in our coupling models. We hypothesize that these structural boundaries act as SSE barriers. Under this hypothesis, strong coupling at the north-central boundary allows large SSEs to rupture across segments, while the creeping, decoupled nature of the central-southern boundary arrests SSE propagation, confining southern SSEs to remain smaller.

6 Summary

This study integrates GNSS-derived inter-slow slip events (SSEs) velocities and reduced-order-modeling (ROM)-accelerated rate-and-state friction SSE-cycle models to investigate the mechanisms controlling along-strike SSE segmentation in the Cascadia subduction zone. The scientific machine learning ROMs enable Markov chain Monte Carlo (MCMC) inversion by reducing the cost of a single model evaluation to ∼30 s on one CPU ($\mathcal{O}(\sim 10^5)$ speedup). Our cycle models indicate that SSE recurrence interval is primarily controlled by low effective normal stress, whereas SSE moment is governed by along-strike variations in inter-SSE coupling within the ETS zone. Mechanically, the inferred effective normal stresses may imply near lithostatic pore fluid pressures governing the Cascadia ETS zone (∼99.3%-99.7%). ROM-MCMC yields mean inter-SSE scaling factors of $\hat{c} \approx 0.64$ in the north, $\hat{c} \approx 0.45$ in central Cascadia, and $\hat{c} \approx 0.38$ in the south, consistent with independently inferred segmented geodetic inter-SEE coupling. Comparing these inter-SSE coupling estimates with long-term coupling indicates that transient SSEs recover most of the slip deficit in the north and south, while a persistent deficit accumulates in central Cascadia, with important implications for seismic and tsunami hazard.

Author contributions:

Conceptualization: YM, AAG, DAM. Methodology: YM, DAM Software: YM, DAM. Data curation: YM. Formal analysis: YM. Investigation: YM. Resources: AAG. Visualization: YM. Validation: AAG, DAM. Supervision: AAG, DAM. Writing—original draft: YM. Writing—review & editing: AAG, DAM. Funding acquisition: YM, AAG.

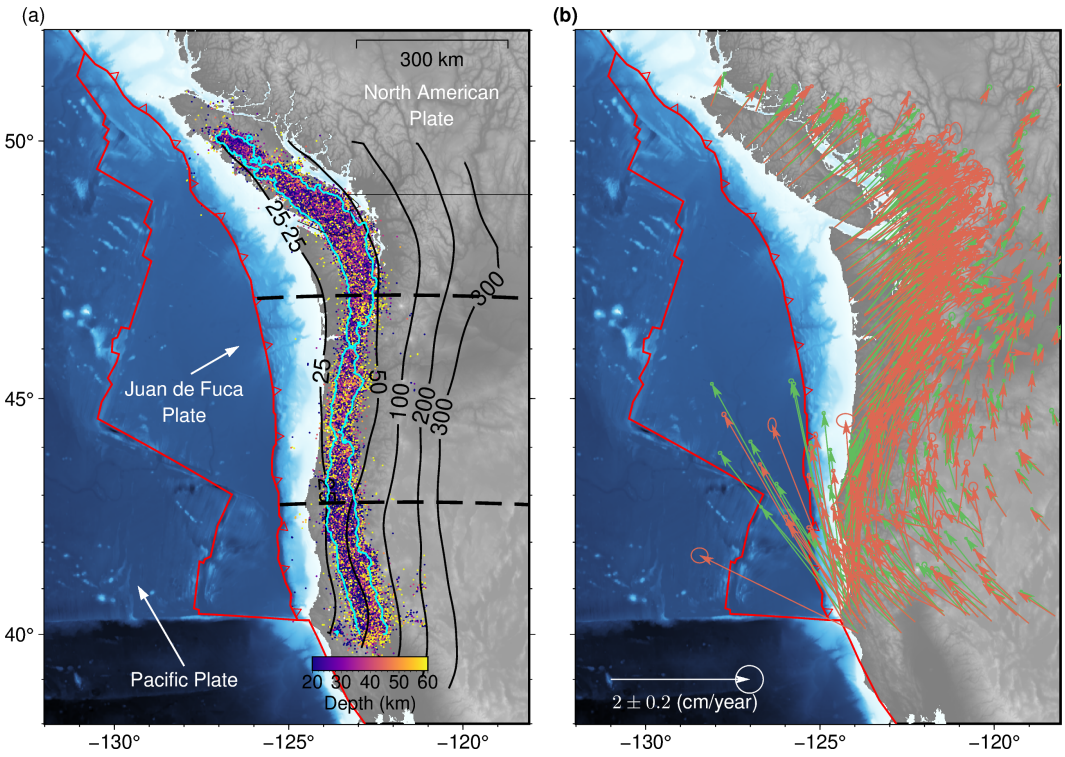

Figure 1. Tectonic settings and Cascadia geodetic GNSS network velocity fields. (a) Tectonic settings of the Cascadia subduction zones: white text and arrows show plate names and motion relative to a fixed North American plate. Red lines mark plate borders. Black contours depict the Cascadia subduction zone interface depth (Hayes et al., 2018). Colored circles show the Cascadia tremor catalog (Wech & Creager, 2008; Wech, 2010). A cyan contour marks the region with over 75 identified tremors in a $0.05^\circ \times 0.05^\circ$ grid, defining the ETS region in this study. Dashed black lines separate northern, central, and southern Cascadia segments. (b) GNSS network velocities: green shows NGL's calculated MIDAS long-term secular velocity, and light red shows the inter-SSE-derived velocity.

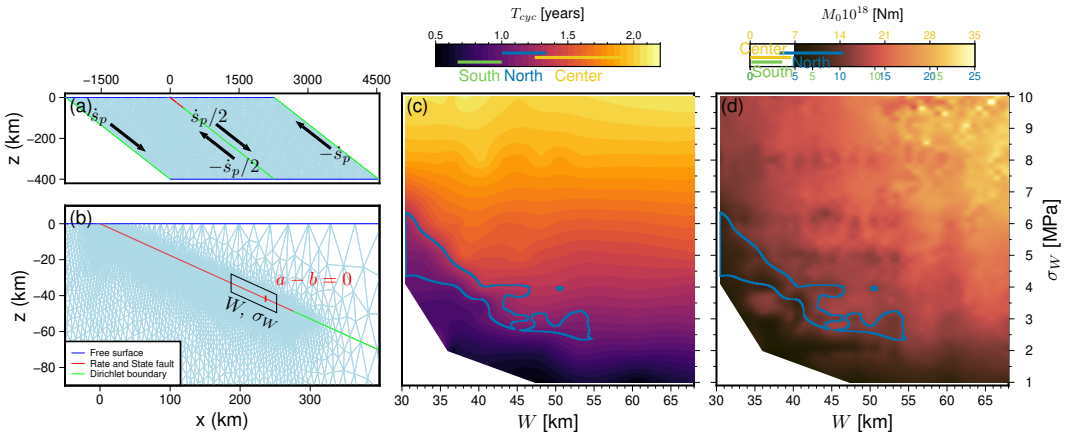

Figure 2. Rate-and-state friction physics-based model settings and ROM parametric exploration. (a) View of the physics-based model computational domain, boundary conditions, and applied loading, where $\dot{s}_P$ is the applied loading rate. Not to scale, note the 4.5× vertical exaggeration of the y-axis. (b) Zoomed view of the rate-and-state friction portion of the megathrust, showing the adaptively refined mesh. Here, W denotes the width of a low effective normal stress zone on the fault, σ_W is the magnitude of the low effective normal stress, and a and b are the constitutive rate-and-state friction parameters controlling the frictional response to sliding velocity and state evolution, respectively. Not to scale, note the 2.5× vertical exaggeration of the y-axis. (c) ROM parametric exploration of the physics-based model using 14,000 $ROM(W^*, \sigma_W^*)$ evaluations. The colors show the SSEs recurrence interval of simulations. In the panel colorbar, the values of observed recurrence interval (Brudzinski & Allen, 2007; Michel et al., 2019) are indicated as blue, yellow, and green lines for north, center, and south Cascadia, respectively. (d) ROM parametric exploration of possible SSE moments, with colors indicating the characteristic moments of the SSE in the simulations. Different colorbar ticks correspond to different Cascadia segments, with observable range values (Michel et al., 2019) indicated as horizontal lines. The blue contour line in panels (c) and (d) shows the possible parameter combination (W, σ_W) that reproduces both the observable SSEs recurrence interval and moment. Note that no combination of parameters reproduces both the recurrence interval and moment for Central and Southern Cascadia.

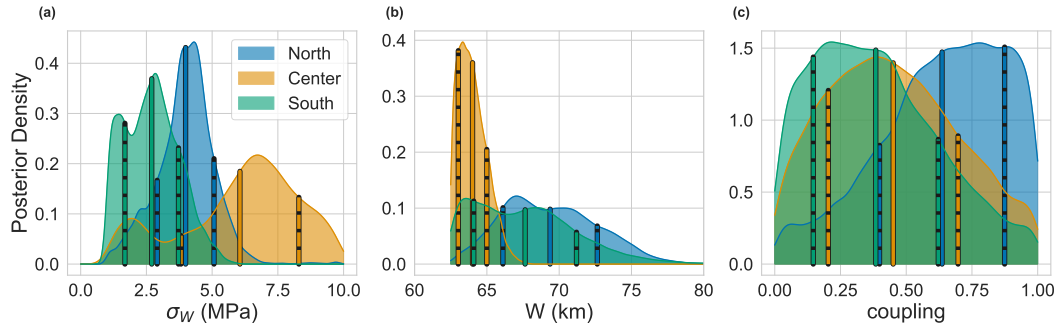

Figure 3. MCMC posterior distribution. We show the results of the MCMC inversion for the posterior distributions of (a) ETS zone width (W), (b) effective normal stress (σ_W), and (c) mean coupling in the ETS zone ($\hat{c}$). The solid and dashed vertical lines indicate, respectively, the expected parameter values and the standard deviations for each region.

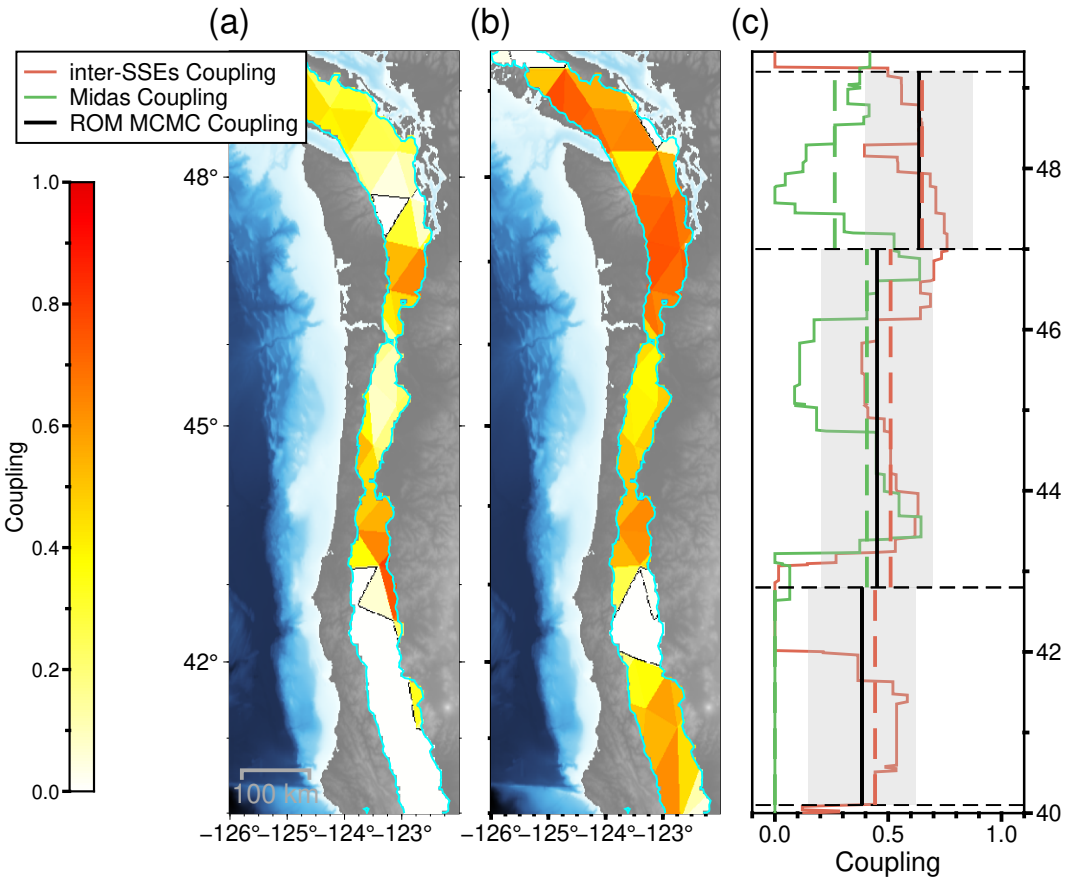

Figure 4. Cascadia ETS zone coupling. (a) Coupling distribution from long-term GNSS station velocities (MIDAS, Blewitt et al., 2018) inverted onto a discretized megathrust mesh. (b) Same as (a), but inverted from our derived inter-SSE GNSS velocities. (c) Along-strike profiles compare geodetic and numerical results. Solid green and red lines show geodetic coupling ($\boldsymbol{c}$), averaged along-dip, for the long-term and inter-SSE fields. Dashed lines show the mean coupling for each segment. The solid black line shows the mean coupling in the ETS zone ($\hat{c}$) inverted by the ROM MCMC inversion. Gray-shaded regions indicate the standard deviation.

Open Research Section

All codes and data products supporting this study are openly available. A Python script to process the NGL GNSS daily data, the input files required to reproduce the `Tandem` simulations, a static version of the `Tandem` code, and the ROM analysis code are publicly hosted on Zenodo (Magen, Gabriel, & May, 2026). The complete raw outputs from all simulations are archived on the National Data Platform S3 bucket. The Zenodo repository provides the direct link and instructions for accessing these raw data. Daily GNSS solutions are available from the Nevada Geodetic Laboratory (Blewitt et al., 2018). The tectonic tremor catalog (Wech & Creager, 2008; Wech, 2010, 2021) can be downloaded from the Pacific Northwest Seismic Network website.

Conflict of Interest declaration

The authors declare no conflicts of interest.

Acknowledgments
This work was supported by Schmidt Science, LLC and the Statewide California Earthquake Center (SCEC, project 25313). DAM and A-AG acknowledge support by the National Science Foundation (NSF) through grant nos. EAR-2121568, OAC-2311208 and RISE-2531036. A-AG acknowledges additional support by the National Science Foundation (grant numbers OAC-2139536, EAR-2225286), by Horizon Europe (ChEESE-2P, grant number 101093038, DT-GEO, grant number 101058129, and Geo-INQUIRE, grant number 101058518), and the National Aeronautics and Space Administration (grant no. 80NSSC20K0495). The authors acknowledge computational support from the National Research Platform via NSF awards CNS-1730158, ACI-1540112, ACI-1541349, OAC-1826967, OAC-2112167, CNS-2100237, CNS-2120019. Additional computing resources were provided by the Institute of Geophysics at LMU Munich (Oeser et al., 2006) and by the Texas Advanced Computing Center (TACC) at The University of Texas at Austin.

References

Andrieu, C., & Thoms, J. (2008, Dec 01). A tutorial on adaptive mcmc. *Statistics and Computing*, *18*(4), 343-373. doi: 10.1007/s11222-008-9110-y

Audet, P., & Bürgmann, R. (2014, June). Possible control of subduction zone slow-earthquake periodicity by silica enrichment. *Nature*, *510*(7505), 389–392. Retrieved 2025-09-09, from `https://www.nature.com/articles/nature13391` (Publisher: Nature Publishing Group) doi: 10.1038/nature13391

Audouze, C., De Vuyst, F., & Nair, P. B. (2009). Reduced-order modeling of parameterized PDEs using time–space-parameter principal component analysis. *International Journal for Numerical Methods in Engineering*, *80*(8), 1025-1057. doi: https://doi.org/10.1002/nme.2540

Bartlow, N. M. (2020). A Long-Term View of Episodic Tremor and Slip in Cascadia. *Geophysical Research Letters*, *47*(3), e2019GL085303. Retrieved 2025-08-20, from `https://onlinelibrary.wiley.com/doi/abs/10.1029/2019GL085303` (_eprint: https://agupubs.onlinelibrary.wiley.com/doi/pdf/10.1029/2019GL085303) doi: 10.1029/2019GL085303

Behr, W. M., & Bürgmann, R. (2021, February). What's down there? The structures, materials and environment of deep-seated slow slip and tremor. *Philosophical Transactions of the Royal Society A: Mathematical, Physical and Engineering Sciences*, *379*(2193), 20200218. Retrieved 2025-09-02, from `https://royalsocietypublishing.org/doi/full/10.1098/rsta.2020.0218` (Publisher: Royal Society) doi: 10.1098/rsta.2020.0218

Benner, P., Gugercin, S., & Willcox, K. (2015). A survey of projection-based model reduction methods for parametric dynamical systems. *SIAM Review*, *57*(4), 483-531. Retrieved from https://doi.org/10.1137/130932715 doi: 10.1137/130932715

Blewitt, G., Hammond, W., & Kreemer, C. (2018, September). Harnessing the gps data explosion for interdisciplinary science. *Eos*, *99*. Retrieved from http://dx.doi.org/10.1029/2018EO104623 doi: 10.1029/2018eo104623

Brown, J. R., Beroza, G. C., Ide, S., Ohta, K., Shelly, D. R., Schwartz, S. Y., ... Kao, H. (2009). Deep low-frequency earthquakes in tremor localize to the plate interface in multiple subduction zones. *Geophysical Research Letters*, *36*(19). Retrieved 2025-09-11, from https://onlinelibrary.wiley.com/doi/abs/10.1029/2009GL040027 (_eprint: https://agupubs.onlinelibrary.wiley.com/doi/pdf/10.1029/2009GL040027) doi: 10.1029/2009GL040027

Brudzinski, M. R., & Allen, R. M. (2007, October). Segmentation in episodic tremor and slip all along Cascadia. *Geology*, *35*(10), 907–910. Retrieved 2025-08-01, from https://doi.org/10.1130/G23740A.1 doi: 10.1130/G23740A.1

Bui-Thanh, T., Damodaran, M., & Willcox, K. (2003, June). Proper orthogonal decomposition extensions for parametric applications in compressible aerodynamics. In *21st AIAA applied aerodynamics conference*. Reston, Virigina: American Institute of Aeronautics and Astronautics.

Bürgmann, R. (2018, August). The geophysics, geology and mechanics of slow fault slip. *Earth and Planetary Science Letters*, *495*, 112–134. Retrieved 2025-01-03, from https://www.sciencedirect.com/science/article/pii/S0012821X18302760 doi: 10.1016/j.epsl.2018.04.062

Carbotte, S. M., Boston, B., Han, S., Shuck, B., Beeson, J., Canales, J. P., ... Gahlawat, R. (2024, June). Subducting plate structure and megathrust morphology from deep seismic imaging linked to earthquake rupture segmentation at Cascadia. *Science Advances*, *10*(23), eadl3198. Retrieved 2025-09-11, from https://www.science.org/doi/10.1126/sciadv.adl3198 (Publisher: American Association for the Advancement of Science) doi: 10.1126/sciadv.adl3198

Cui, T., Marzouk, Y. M., & Willcox, K. E. (2015). Data-driven model reduction for the bayesian solution of inverse problems. *International Journal for Numerical Methods in Engineering*, *102*(5), 966-990. doi: https://doi.org/10.1002/nme.4748

Dascher-Cousineau, K., & Bürgmann, R. (2024). Global subduction slow slip events and associated earthquakes. *Science Advances*, *10*(35), eado2191. doi: 10.1126/sciadv.ado2191

Degen, D., Caviedes Voullième, D., Buiter, S., Hendricks Franssen, H.-J., Vereecken, H., González-Nicolás, A., & Wellmann, F. (2023). Perspectives of physics-based machine learning strategies for geoscientific applications governed by partial differential equations. *Geoscientific Model Development*, *16*(24), 7375–7409.

DeMets, C., Gordon, R. G., & Argus, D. F. (2010, 04). Geologically current plate motions. *Geophysical Journal International*, *181*(1), 1-80. doi: 10.1111/j.1365-246X.2009.04491.x

Dieterich, J. H. (1979). Modeling of rock friction: 1. Experimental results and constitutive equations. *Journal of Geophysical Research: Solid Earth*, *84*(B5), 2161-2168. doi: https://doi.org/10.1029/JB084iB05p02161

Dragert, H., Wang, K., & James, T. S. (2001, May). A Silent Slip Event on the Deeper Cascadia Subduction Interface. *Science*, *292*(5521), 1525–1528. Retrieved 2025-09-11, from https://www.science.org/doi/10.1126/science.1060152 (Publisher: American Association for the Advancement of Science) doi: 10.1126/science.1060152

Gabriel, A.-A., Karki, P., Magen, Y., Oryan, B., Ulrich, T., Yun, J., & May, D. A. (2025). Tandem: An open-source high-performance computing volumetric software to model sequences of earthquakes and aseismic slip across complex fault systems.

Gelman, A., & Rubin, D. B. (1992, November). Inference from iterative simulation using multiple sequences. *Stat. Sci.*, *7*(4), 457–472.

Goldfinger, C., Beeson, J., Black, B., Vizcaino, A., Nelson, C., Morey, A., ... Walzcak, M. (2025, 09). Unravelling the dance of earthquakes: Evidence of partial synchronization of the northern san andreas fault and cascadia megathrust. *Geosphere*, *21*(6), 1132-1180. Retrieved from `https://doi.org/10.1130/GES02857.1` doi: 10.1130/GES02857.1

Gomberg, J., Wech, A., Creager, K., Obara, K., & Agnew, D. (2016). Reconsidering earthquake scaling. *Geophysical Research Letters*, *43*(12), 6243–6251. Retrieved 2025-09-02, from `https://onlinelibrary.wiley.com/doi/abs/10.1002/2016GL069967` (_eprint: https://agupubs.onlinelibrary.wiley.com/doi/pdf/10.1002/2016GL069967) doi: 10.1002/2016GL069967

Gualandi, A. (2025, August). Near real-time Cascadia slow slip events. *Geophysical Journal International*, *242*(2), ggaf198. Retrieved 2025-08-22, from `https://doi.org/10.1093/gji/ggaf198` doi: 10.1093/gji/ggaf198

Hastings, W. K. (1970, 04). Monte Carlo sampling methods using Markov chains and their applications. *Biometrika*, *57*(1), 97-109. doi: 10.1093/biomet/57.1.97

Hayes, G. P., Moore, G. L., Portner, D. E., Hearne, M., Flamme, H., Furtney, M., & Smoczyk, G. M. (2018). Slab2, a comprehensive subduction zone geometry model. *Science*, *362*(6410), 58-61. doi: 10.1126/science.aat4723

Hobson, G. M., & May, D. A. (2025). Sensitivity analysis of the thermal structure within subduction zones using reduced-order modeling. *Geochemistry, Geophysics, Geosystems*, *26*(5), e2024GC011937. doi: https://doi.org/10.1029/2024GC011937

Ide, S., & Beroza, G. C. (2023, August). Slow earthquake scaling reconsidered as a boundary between distinct modes of rupture propagation. *Proceedings of the National Academy of Sciences*, *120*(32), e2222102120. Retrieved 2025-09-02, from `https://pnas.org/doi/10.1073/pnas.2222102120` doi: 10.1073/pnas.2222102120

Jr., F. J. M. (1951). The kolmogorov-smirnov test for goodness of fit. *Journal of the American Statistical Association*, *46*(253), 68–78. doi: 10.1080/01621459.1951.10500769

Kaveh, H., Avouac, J. P., & Stuart, A. M. (2024, 11). Spatiotemporal forecast of extreme events in a chaotic model of slow slip events. *Geophysical Journal International*, *240*(2), 870-885. doi: 10.1093/gji/ggae417

Lapusta, N., Rice, J. R., Ben-Zion, Y., & Zheng, G. (2000). Elastodynamic analysis for slow tectonic loading with spontaneous rupture episodes on faults with rate- and state-dependent friction. *Journal of Geophysical Research: Solid Earth*, *105*(B10), 23765-23789. doi: https://doi.org/10.1029/2000JB900250

Li, D., & Liu, Y. (2016). Spatiotemporal evolution of slow slip events in a nonplanar fault model for northern Cascadia subduction zone. *Journal of Geophysical Research: Solid Earth*, *121*(9), 6828-6845. doi: https://doi.org/10.1002/2016JB012857

Li, D., & Liu, Y. (2017). Modeling slow-slip segmentation in cascadia subduction zone constrained by tremor locations and gravity anomalies. *Journal of Geophysical Research: Solid Earth*, *122*(4), 3138-3157. doi: https://doi.org/10.1002/2016JB013778

Lindsey, E. O., Mallick, R., Hubbard, J. A., Bradley, K. E., Almeida, R. V., Moore, J. D. P., ... Hill, E. M. (2021, May). Slip rate deficit and earthquake poten-

tial on shallow megathrusts. *Nature Geoscience*, *14*(5), 321–326. Retrieved 2025-09-02, from https://www.nature.com/articles/s41561-021-00736-x (Publisher: Nature Publishing Group) doi: 10.1038/s41561-021-00736-x

Liu, Y., & Rice, J. R. (2007). Spontaneous and triggered aseismic deformation transients in a subduction fault model. *Journal of Geophysical Research: Solid Earth*, *112*(B9).

Liu, Y., & Rice, J. R. (2009). Slow slip predictions based on granite and gabbro friction data compared to GPS measurements in northern Cascadia. *Journal of Geophysical Research: Solid Earth*, *114*(B9).

Luo, Y., & Ampuero, J.-P. (2018). Stability of faults with heterogeneous friction properties and effective normal stress. *Tectonophysics*, *733*, 257-272. doi: https://doi.org/10.1016/j.tecto.2017.11.006

Luo, Y., & Liu, Z. (2019). Slow-slip recurrent pattern changes: Perturbation responding and possible scenarios of precursor toward a megathrust earthquake. *Geochemistry, Geophysics, Geosystems*, *20*(2), 852-871. doi: https://doi.org/10.1029/2018GC008021

Luo, Y., & Liu, Z. (2021, March). Fault zone heterogeneities explain depth-dependent pattern and evolution of slow earthquakes in Cascadia. *Nature Communications*, *12*(1), 1959. Retrieved 2025-09-11, from https://www.nature.com/articles/s41467-021-22232-x (Publisher: Nature Publishing Group) doi: 10.1038/s41467-021-22232-x

Magen, Y., Gabriel, A.-A., & May, D. (2026). *Coupling heterogeneity in the cascadia slow-slip zone from GNSS inversion and reduced-order modeling-accelerated rate-and-state friction simulations code and data.* Zenodo. doi: https://doi.org/10.5281/zenodo.18353479

Magen, Y., May, D. A., & Gabriel, A.-A. (2026, 01). Reduced-order modelling of cascadia's slow slip cycles. *Geophysical Journal International*, ggag050. Retrieved from https://doi.org/10.1093/gji/ggag050 doi: 10.1093/gji/ggag050

Michel, S., Gualandi, A., & Avouac, J.-P. (2019, September). Interseismic Coupling and Slow Slip Events on the Cascadia Megathrust. *Pure and Applied Geophysics*, *176*(9), 3867–3891. Retrieved from https://doi.org/10.1007/s00024-018-1991-x doi: 10.1007/s00024-018-1991-x

Michel, S., Jolivet, R., Klein, E., & Maubant, L. (2025). 14 years of slip on the hikurangi subduction zone. *Journal of Geophysical Research: Solid Earth*, *130*(7), e2024JB030865. doi: https://doi.org/10.1029/2024JB030865

Morton, E. A., Bilek, S. L., & Rowe, C. A. (2023). Cascadia Subduction Zone Fault Heterogeneities From Newly Detected Small Magnitude Earthquakes. *Journal of Geophysical Research: Solid Earth*, *128*(6), e2023JB026607. Retrieved 2025-09-12, from https://onlinelibrary.wiley.com/doi/abs/10.1029/2023JB026607 (_eprint: https://agupubs.onlinelibrary.wiley.com/doi/pdf/10.1029/2023JB026607) doi: 10.1029/2023JB026607

Mosegaard, K., & Tarantola, A. (1995). Monte carlo sampling of solutions to inverse problems. *Journal of Geophysical Research: Solid Earth*, *100*(B7), 12431-12447.

Nikkhoo, M., & Walter, T. R. (2015, 03). Triangular dislocation: an analytical, artefact-free solution. *Geophysical Journal International*, *201*(2), 1119-1141. Retrieved from https://doi.org/10.1093/gji/ggv035 doi: 10.1093/gji/ggv035

Nuyen, C., & Schmidt, D. (2024, Jun.). Along-strike changes in ets behavior near the slab edge of southern cascadia. *Seismica*, *2*(4). Retrieved from https://seismica.library.mcgill.ca/article/view/1097 doi: 10.26443/seismica.v2i4.1097

Oeser, J., Bunge, H.-P., & Mohr, M. (2006). Cluster design in the earth sciences

tethys. In *International conference on high performance computing and communications* (pp. 31–40).

Okada, Y. (1992). Internal deformation due to shear and tensile faults in a half-space. *Bulletin of the seismological society of America*, *82*(2), 1018–1040.

Ozawa, S., Dunham, E. M., & Condit, C. (2025, August). *Metamorphic dehydration, fluid pressure, and the frictional-viscous transition along subduction megathrusts: Case study in cascadia and implications for slow earthquakes.*

Peng, Z., & Gomberg, J. (2010, September). An integrated perspective of the continuum between earthquakes and slow-slip phenomena. *Nature Geoscience*, *3*(9), 599–607. Retrieved 2025-09-16, from `https://www.nature.com/articles/ngeo940` (Publisher: Nature Publishing Group) doi: 10.1038/ngeo940

Perez-Silva, A., Kaneko, Y., Savage, M., Wallace, L., & Warren-Smith, E. (2023). Characteristics of slow slip events explained by rate-strengthening faults subject to periodic pore fluid pressure changes. *Journal of Geophysical Research: Solid Earth*, *128*(6), e2022JB026332. doi: https://doi.org/10.1029/2022JB026332

Rekoske, J. M., Gabriel, A.-A., & May, D. A. (2023, August). Instantaneous physics-based ground motion maps using reduced-order modeling. *Journal of Geophysical Research: Solid Earth*, *128*(8).

Rekoske, J. M., May, D. A., & Gabriel, A.-A. (2025, 02). Reduced-order modelling for complex three-dimensional seismic wave propagation. *Geophysical Journal International*, *241*(1), 526-548. doi: 10.1093/gji/ggaf049

Rice, J. R., & Ben-Zion, Y. (1996). Slip complexity in earthquake fault models. *Proceedings of the National Academy of Sciences*, *93*(9), 3811-3818. doi: 10.1073/pnas.93.9.3811

Rogers, G., & Dragert, H. (2003, June). Episodic Tremor and Slip on the Cascadia Subduction Zone: The Chatter of Silent Slip. *Science*, *300*(5627), 1942–1943. Retrieved 2025-01-03, from `https://www.science.org/doi/full/10.1126/science.1084783` (Publisher: American Association for the Advancement of Science) doi: 10.1126/science.1084783

Rubin, A. M. (2008). Episodic slow slip events and rate-and-state friction. *Journal of Geophysical Research: Solid Earth*, *113*(B11).

Ruina, A. (1983). Slip instability and state variable friction laws. *Journal of Geophysical Research: Solid Earth*, *88*(B12), 10359-10370. doi: https://doi.org/10.1029/JB088iB12p10359

Saux, J. P., Molitors Bergman, E. G., Evans, E. L., & Loveless, J. P. (2022). The role of slow slip events in the cascadia subduction zone earthquake cycle. *Journal of Geophysical Research: Solid Earth*, *127*(2), e2021JB022425. doi: https://doi.org/10.1029/2021JB022425

Savage, J. C. (1983). A dislocation model of strain accumulation and release at a subduction zone. *Journal of Geophysical Research: Solid Earth*, *88*(B6), 4984-4996. doi: https://doi.org/10.1029/JB088iB06p04984

Schmalzle, G. M., McCaffrey, R., & Creager, K. C. (2014, April). Central Cascadia subduction zone creep. *Geochemistry, Geophysics, Geosystems*, *15*(4), 1515–1532. Retrieved 2025-09-02, from `https://doi.org/10.1002/2013GC005172` (Publisher: John Wiley & Sons, Ltd) doi: 10.1002/2013GC005172

Segall, P., Rubin, A. M., Bradley, A. M., & Rice, J. R. (2010). Dilatant strengthening as a mechanism for slow slip events. *Journal of Geophysical Research: Solid Earth*, *115*(B12). doi: https://doi.org/10.1029/2010JB007449

Sirovich, L. (1987). Turbulence and the dynamics of coherent structures. i. coherent structures. *Quart. Appl. Math.*, *45*(3), 561–571.

Tarantola, A. (2005). *Inverse problem theory and methods for model parameter estimation.* SIAM.

Uphoff, C., May, D. A., & Gabriel, A.-A. (2022, 11). A discontinuous Galerkin method for sequences of earthquakes and aseismic slip on multiple faults using

unstructured curvilinear grids. *Geophysical Journal International*, *233*(1), 586-626. doi: 10.1093/gji/ggac467

Walton, M. A., Staisch, L. M., Dura, T., Pearl, J. K., Sherrod, B., Gomberg, J., ... Wirth, E. (2021). Toward an integrative geological and geophysical view of cascadia subduction zone earthquakes [Journal Article]. *Annual Review of Earth and Planetary Sciences*, *49*(Volume 49, 2021), 367-398. doi: https://doi.org/10.1146/annurev-earth-071620-065605

Wang, P.-L., Engelhart, S. E., Wang, K., Hawkes, A. D., Horton, B. P., Nelson, A. R., & Witter, R. C. (2013). Heterogeneous rupture in the great Cascadia earthquake of 1700 inferred from coastal subsidence estimates. *Journal of Geophysical Research: Solid Earth*, *118*(5), 2460–2473. Retrieved 2025-09-12, from `https://onlinelibrary.wiley.com/doi/abs/10.1002/jgrb.50101` (_eprint: https://agupubs.onlinelibrary.wiley.com/doi/pdf/10.1002/jgrb.50101) doi: 10.1002/jgrb.50101

Watt, J. T., & Brothers, D. S. (2020, November). Systematic characterization of morphotectonic variability along the Cascadia convergent margin: Implications for shallow megathrust behavior and tsunami hazards. *Geosphere*, *17*(1), 95–117. Retrieved 2025-09-12, from `https://doi.org/10.1130/GES02178.1` doi: 10.1130/GES02178.1

Wech, A. G. (2010, 07). Interactive tremor monitoring. *Seismological Research Letters*, *81*(4), 664-669. doi: 10.1785/gssrl.81.4.664

Wech, A. G. (2021). Cataloging tectonic tremor energy radiation in the cascadia subduction zone. *Journal of Geophysical Research: Solid Earth*, *126*(10), e2021JB022523. doi: https://doi.org/10.1029/2021JB022523

Wech, A. G., & Creager, K. C. (2008). Automated detection and location of Cascadia tremor. *Geophysical Research Letters*, *35*(20). doi: https://doi.org/10.1029/2008GL035458

Zhang, S., & Houston, H. (2025). Evidence for stress diffusion and along-strike segmentation in cascadia tremor migrations lasting minutes to weeks. *AGU Advances*, *6*(5), e2025AV001746. doi: https://doi.org/10.1029/2025AV001746

Zhu, C., Byrd, R. H., Lu, P., & Nocedal, J. (1997, December). Algorithm 778: L-bfgs-b: Fortran subroutines for large-scale bound-constrained optimization. *ACM Trans. Math. Softw.*, *23*(4), 550–560. doi: 10.1145/279232.279236

Supporting Information for "Along-strike coupling heterogeneity in Cascadia's slow-slip zone constrained by GNSS and reduced-order rate-and-state modeling"

Yohai Magen[1], Alice-Agnes Gabriel[1,2], Dave A. May[1]

[1]Institute of Geophysics and Planetary Physics, Scripps Institution of Oceanography, University of California, San Diego, CA, USA
[2]Department of Earth and Environmental Sciences, Ludwig-Maximilians-Universität München, Munich, Germany

Contents of this file

S1 GNSS Data and Processing

To calculate the inter-SSEs velocity field in Cascadia, we collected daily time series from an 820 GNSS station processed by the Nevada Geodetic Laboratory (Blewitt et al., 2018). We generally followed the processing change suggested by Bartlow (2020) to separate the SSE contribution from other contributions to the GNSS daily displacement time series. We extended the processing up to August 1^{st} 2025 and used it to invert the inter-SSE coupling within the ETS zone.

We downloaded data from all available stations whose locations fell within the longitude range of -127° to -118° and the latitude range of 40° to 55°. All station positions are referenced to the global IGS20 with a fixed North American reference frame. We then preprocess the raw daily GNSS position time series to mitigate noise and correct for non-tectonic signals. The process begins by filtering out stations with fewer than 100 days of data. For the remaining stations, we first identify and remove outliers using a 20-day moving-median window filter. Following outlier removal, we correct for step-discontinuities from two primary sources. We address non-tectonic offsets, such as those from equipment changes documented by the Nevada Geodetic Laboratory, and then correct for coseismic offsets from a regional earthquake for all earthquakes with $M_w \geq 5.5$ in the US Geological Survey earthquake catalog in the region. For each earthquake, stations are considered for correction if they fall within a magnitude-dependent empirical radius of influence, calculated as 10^{M_w} $1.5{\cdot}10^4$, where M_w is the earthquake moment magnitude. In all cases, the offset is quantified as the difference between the median positions of the data windows immediately preceding and following the event. This value is subtracted from the subsequent time series to ensure continuity. We continued to remove sites near Mount St. Helens, which exhibit non-negligible volcanic deformation (see Table S1). We then considered only stations with at least 4 years of data, excluding time periods with data gaps exceeding 6 months. If a station contained a single large gap, we retained the longest continuous segment for analysis, provided it still met the minimum duration requirement of four years. Following this initial preprocessing stage, we have 458 GNSS stations with time series cleaned of outliers, non-tectonic and regional earthquake offsets, and at least 4 years of data.

To isolate signals related to the inter-SSEs secular velocity, we modeled each GNSS time series separately using linear least-squares inversion to separate the long-term secular velocity from transient SSE motion and seasonal contributions. To achieve this, we added a Heaviside step function to the least square fit whenever the number of tectonic tremors out of the Pacific Northwest Seismic Network tectonic tremor catalog (Wech, 2021; Wech & Creager, 2008; Wech, 2010) in the empirical proximity to the station exceeded a certain threshold, where the tremors serve as a proxy for possible slow slip. For each station, we considered all tremors within a 250 km radius and flagged any day with 50 or more tremor detections. For all continuous flagged dates of 6 or more days (Figure S1), we masked those dates from the position time series and added the Heaviside function at the midpoint of the continuous ETS time interval (Figure S2).

$$d(t) = d_0 + vt + s_1\sin(2\pi t) + s_2\cos(2\pi t) + s_3\sin(4\pi t) + s_4\cos(4\pi t) + \sum_{m=1}^{n} \Delta d_m H(t - t_m) \quad \text{(S1)}$$

Where v is the station inter-SSEs secular velocity, s_i, $i \in [1, 2, 3, 4]$ are annual and semi-annual seasonal terms, H is a Heaviside function, and Δd_m is the size of the step related to the m^{th} identified ETS time period in a specific station.

From the modeled parameters, we calculated the inter-SSEs secular velocity field (Figure 1) by directly extracting the linear rate (v) term from the least-squares fit to the time-series data. To estimate the uncertainties in these velocities, we used bootstrap re-

sampling. For each station, we repeated the entire least-squares inversion process 20 times, using a random 80% subset of the interseismic data each time. The final reported velocities are the mean of these 20 iterations, and the uncertainties are reported as the standard deviation. Following the completion of the analysis of all 458 GNSS stations, we visually inspect the data and screen out an additional 12 stations in which our processing chain yields unrealistic velocities in at least one station component (East-West, North-South, Up-Down).

To ensure the robustness of our derived velocity field, we performed a sensitivity analysis on the ETS detection parameters. We vary the tremor-count threshold (30-80 tremors/day), the search radius around the station (200-300 km), and the minimum number of consecutive days required for an ETS (3-10 days), yielding an ensemble of 530 distinct velocity fields. We quantified the stability of the velocity field by calculating the difference between the 95^{th} and the 5^{th} percentiles for each velocity component at each station (Figure S4). The resulting velocity field is highly stable with respect to the choice of detection parameters, with a mean variability of $\sim$0.003, $\sim$0.002, and $\sim$0.006 mm/year for the East-West, North-South, and Up-Down components, respectively. We observed a maximum outlier variability of $\sim$0.3 mm/year in the East-West component of station P161. This sensitivity test validates that the derived inter-SSEs velocity field is insensitive to the choice of specific ETS detection parameters.

S2 Geodetic Inversion for ETS zone Coupling

We invert the Cascadia geodetic velocity fields to infer the distribution of interseismic coupling along the Cascadia subduction megatrust. To discretize the subduction interface, we use high-resolution 3D point-cloud data from the Slab2.0 (Hayes et al., 2018) model for the Cascadia region. We first downsample the raw data using a spatially weighted resampling algorithm that maintains higher point density in regions where the slab is closer to the onshore GNSS network, ensuring optimal model sensitivity. Using these resampled coordinates, we generate a three-dimensional curved mesh through a Delaunay triangulation. To ensure a physically realistic fault surface, we filter the resulting mesh by removing triangles with edge lengths exceeding 2.5°, thereby eliminating artifacts at the grid boundaries. This process yields a final fault mesh comprising 232 triangular elements that accurately capture the non-planar geometry of the megathrust while remaining computationally efficient for subsequent inversions.

The inversion solves for a spatially variable coupling coefficient, c, and a rake angle, θ, for each triangular patch. We employ a two-step procedure, a preliminary least-squares inversion for backslip components is used to generate a starting model for a subsequent, non-linear inversion for coupling and rake.

In the first step, we solve for the backslip (i.e., slip deficit rate, Savage (1983)) along the Cascadia subduction zone by minimizing the following objective function:

$$\underset{\boldsymbol{m}}{\operatorname{argmin}} \left(\|\boldsymbol{A}\boldsymbol{m} - \boldsymbol{d}\|_2^2 + \beta^2 \|\boldsymbol{D}\boldsymbol{m}\|_2^2 \right) \tag{S2}$$

where $\boldsymbol{A}$ are the elastic Green's function matrix derived from Okada (1992) solutions for triangular dislocations (Nikkhoo & Walter, 2015), $\boldsymbol{m} = (\boldsymbol{m}_{ss}, \boldsymbol{m}_{ds})$ denotes the strike-slip and dip-slip backslip components on the fault patches, $\boldsymbol{d}$ are the observed GNSS velocities, $\boldsymbol{D}$ is the discrete first finite difference derivative matrix, which penalizes roughness in the slip distribution, and β is a parameter contorting the slip smoothing. The optimal value for β is selected by analyzing the trade-off curve between model misfit and solution roughness (L-curve).

The second inversion step is implemented as a constrained optimization problem. The results of the first inversion step are used to derive an initial guess for the coupling and rake of each patch:

$$\boldsymbol{\theta}_i = \operatorname{atan2}(\boldsymbol{m}_{ds}, \boldsymbol{m}_{ss}) \tag{S3}$$

and

$$\boldsymbol{c} = \max\left(\boldsymbol{0}, \boldsymbol{1} - \frac{\sqrt{\boldsymbol{m}_{ds}^2 + \boldsymbol{m}_{ss}^2}}{|V_{pl}|}\right) \tag{S4}$$

where $|V_{pl}|$ is the magnitude of the plate convergence rate of 3.7 cm/year (DeMets et al., 2010). We then solve the same minimization problem (Eq. S2) using the L-BFGS-B algorithm (Zhu et al., 1997) to find the optimal coupling ($0 \leq c \leq 1$) and rake (θ) for each patch. The backslip vector $\boldsymbol{m}$ is now parameterized as:

$$\boldsymbol{m}_{ss} = \boldsymbol{c} \cdot |V_{pl}| \cdot \cos(\boldsymbol{\theta}) \tag{S5}$$

and

$$\boldsymbol{m}_{ds} = \boldsymbol{c} \cdot |V_{pl}| \cdot \sin(\boldsymbol{\theta}) \tag{S6}$$

Here, the rake angle θ is defined counter-clockwise from the strike direction, such that $\theta = 90°$ corresponds to pure thrust motion.

We apply this inversion procedure independently to two different velocity fields. The first inversion uses the inter-SSEs velocity field derived in Text S1. The second inversion uses the MIDAS GNSS velocity solution (Blewitt et al., 2018).

To quantify our model uncertainties, we assume that the model and GNSS uncertainties are uncorrelated and follow a Gaussian distribution. The data covariance matrix can be written as a diagonal matrix $\boldsymbol{C}_d$ where diag($\boldsymbol{C}_d$) are the GNSS uncertainties. The model uncertainties can then be calculated by (Tarantola, 2005):

$$\boldsymbol{C}_m = \boldsymbol{A}^T \boldsymbol{C}_d^{-1} \boldsymbol{A} \tag{S7}$$

The model uncertainties estimation is shown in Figure S5.

S3 Cascadia SSEs numerical simulations

We perform a two-dimensional quasi-dynamic simulation of SSEs cycles in CSZ-like settings. The fault stress evolution in this model follows the regularized form of the rate-and-state friction law (Dieterich, 1979; Ruina, 1983; Lapusta et al., 2000; Rice & Ben-Zion, 1996), given by

$$\tau(\dot{s}, \psi) = a \operatorname{arcsinh}\left(\frac{\dot{s}}{2\dot{s}_0} \exp\left(\frac{\psi}{a}\right)\right) \tag{S8}$$

where the fault shear stress τ is a function of the slip-rate $\dot{s}$ and a state variable ψ, with a representing an empirical friction parameter to describe the "direct effect" and $\dot{s}_0$ a reference slip-rate. The state variable evolves temporally according to the Dietrich-Ruina aging law

$$\frac{d\psi}{dt}(\dot{s}, \psi) = \frac{b\dot{s}_0}{L}\left(\exp\left(\frac{f_0 - \psi}{b}\right) - \frac{\dot{s}}{\dot{s}_0}\right) \tag{S9}$$

where b is an empirical frictional parameter describing the time-dependent "evolution" effect, L denotes the characteristic slip distance, and f_0 is a reference friction coefficient.

All full order physics based simulations in this study consist of two-dimensional parallelogram-shaped domains measuring 4500 km in length and 400 km in width, containing a single planar fault that bisects the domain into two geometrically identical regions (Figure 1). To approximate the CSZ, both the fault and lateral domain boundaries are inclined at a shallow dip angle of 10° relative to the upper and lower domain free surface boundaries. We prescribed Loading as steady tectonic convergence (Figure 1), imposed via Dirichlet boundary conditions, with velocities of $V_p = 3.7$ cm/year to the fault at depths exceeding 280 km along-dip and $\pm V_p/2$ at the domain right and left boundaries.

SSEs arise spontaneously in rate-and-state friction models from specific combinations of frictional stability regimes along the fault, particularly including a conditionally stable region near the transition between fully locked and continuously creeping sections. These models incorporate a fault portion with reduced effective normal stress (e.g., Liu & Rice, 2009; Li & Liu, 2016; Rubin, 2008; Luo & Ampuero, 2018). We follow a similar setup to Liu and Rice (2009), applying transitional frictional stability near the down-dip limit of the seismogenic zone with a reduced effective normal stress of σ_W over a region of W km width (Figure 1a).

We employ the open-source SEAS simulation software `Tandem` (Uphoff et al., 2022) to conduct quasi-dynamic simulations of SSEs in this two-dimensional Cascadia-like setting (Liu & Rice, 2009). Each simulation constitutes a full-order model (FOM), in which the simulation is run for at least 30 SSE cycles following a spin-up phase of 110 years. We conducted 110 distinct simulations across a parametric space with W ranging from 30.5 to 68 km and σ_W from 1 to 10 MPa. This included an additional 34 simulations beyond those presented in Magen, May, and Gabriel (2026), which were necessary to resolve longer recurrence intervals, as observed in central Cascadia.

S4 Reduced-Order Modeling and MCMC Inversion Details

To construct the reduced-order model (ROM), we initially sample the W and σ_W parametric space uniformly, and then refine the sampling in regions of low reconstruction fidelity during the construction process. For each forward simulation, we compress the temporal evolution of slip, slip rate, and state variables at 280 observation points along the megathrust into a compact fixed-length vector. By stacking the 110 fixed-length vectors, we create a single data matrix. To efficiently interpolate between the matrix rows (the simulation's vector representation), we perform a Proper Orthogonal Decomposition (POD, Bui-Thanh et al., 2003) that decomposes the data matrix into basis vectors and coefficients. Thus, POD represents this matrix in a reduced basis and allows us to

obtain the corresponding modal coefficients. Finally, we interpolate the coefficients using radial basis functions (Audouze et al., 2009) to predict the coefficients of any (W^*, σ_W^*) pair that falls within the training W and σ_W intervals but was not simulated.

During the Markov Chain Monte Carlo (MCMC) inference stage, we perform independent inversions for each Cascadia segment (north, central, south). We run 10 parallel chains of 4000 iterations using an adaptive Gaussian proposal distribution tuned during a 10% burn-in period (Andrieu & Thoms, 2008). Convergence is assessed using the Gelman-Rubin potential scale reduction factor, which compares variance across the 10 chains to that in a single chain (Gelman & Rubin, 1992). Convergence is achieved for all parameters (Gelman-Rubin factor ≤ 1.02), with an effective sample size exceeding 400, supporting robust sampling of the posterior distribution.

S5 Extraction of SSE Characteristics and Tremor Zone Width for MCMC Inversion

To constrain the posterior probability distributions in our MCMC inversion (Section 3), we extract observational priors and likelihood parameters for SSEs characteristics and ETS-zone widths across the Cascadia margin. The margin is partitioned into three segments based on latitude: southern ($40.1° \leq$ latitude $< 44.0°$), central ($44.0° \leq$ latitude $< 47.0°$), and northern ($47.0° \leq$ latitude $< 49.2°$)).

We derive the observed SSE recurrence intervals (T_c^{obs}) and characteristic moments (M_0^{obs}) using the SSEs event catalog and the spatiotemporal moment rate data from Michel et al. (2019, see Figure S8). To avoid over-counting segmented or overlapping signals, events occurring within one month of each other within the same region are merged. The moment rate is integrated over time and space using the trapezoidal rule to calculate total moment release. The regional recurrence intervals are calculated as the mean temporal difference between consecutive events and compared to values derived from tectonic tremors observations (Brudzinski & Allen, 2007, see Table S1), while the characteristic moments are derived from the mean and standard deviation of the regional M_0 distributions.

To define the prior distributions for the ETS-zone width (W), we analyze the spatial density of the regional tectonic tremor catalog (Wech & Creager, 2008; Wech, 2010, 2021). We calculate a map view tremor density grid with a $0.05°$ spatial resolution (Figure S9). Margin-perpendicular density profiles are then extracted along constant latitudes. For each extracted profile, we fit a second-order polynomial to the tremor density distribution (Figure S10. The local width of the tremor band is defined as the geodesic distance (in km) between the symmetric points of the parabola, which is equal to 75 tremors, and is then projected onto the slab interface. Then we calculate the mean and standard deviation of the widths for each segment (Figure S11 which are used as prior $W \sim \mathcal{N}(\mu, \sigma)$.

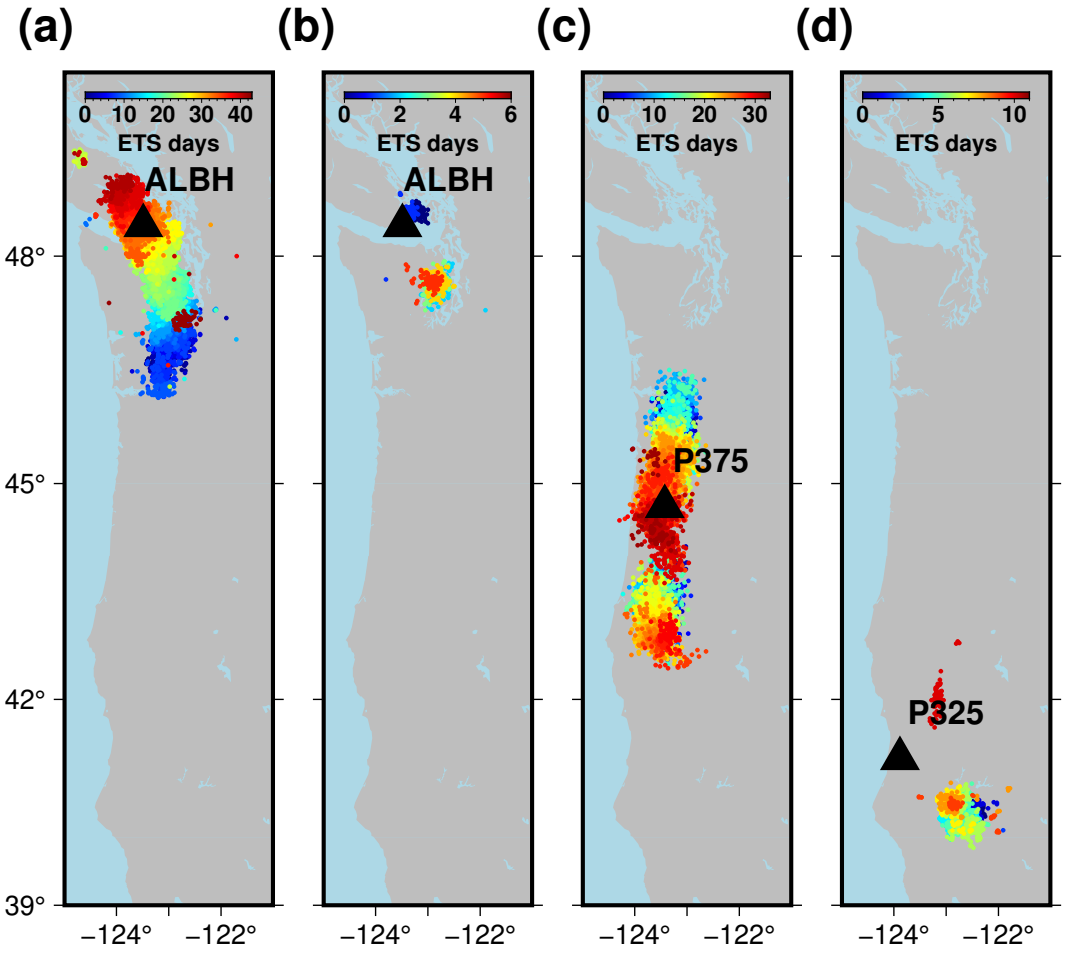

Figure S1. Map view of 4 examples of ETS sequences defined to trigger an ETS offset in the respective station time series. The black triangle and text show the station location and a four-character identification code. Tectonic tremors are plotted as circles colored according to time of occurrence since the start of the ETS event. (a) The longest ETS found with respect to the station ALBH (b), The shortest ETS found with respect to the station ALBH (c), The longest ETS found with respect to the station P375 (d). The median length ETS found with respect to the station P325

Table S1. Cascadia SSEs segments characteristics

Region	Recurrence (months)[a]	Recurrence (months)	Moment ($\times 10^{18}$ Nm)	M_w
North	14 ± 2	13.52 ± 1.4	8.25 ± 3.29	6.58
Center	19 ± 4	20.5 ± 3.7	5.22 ± 3.5	6.45
South	10 ± 2	7.0 ± 4.0	1.33 ± 1.23	6.05

[a]Brudzinski and Allen (2007)

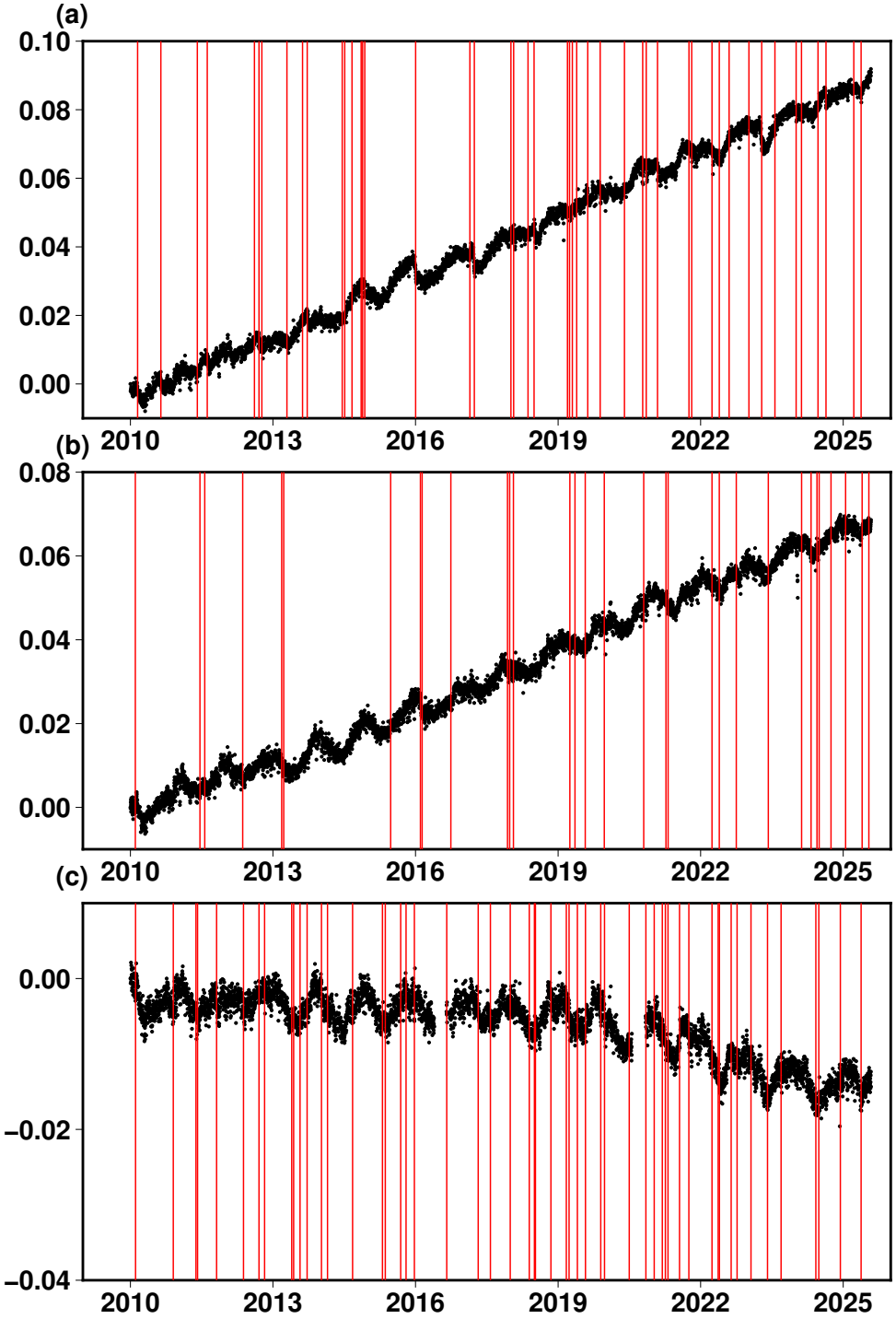

Figure S2. Example of identified ETSs in 3 E-W time series, red vertical line shows the mid date of an identified ETS. (a) E-W displacement of station ALBH (b) E-W displacement of station P375 (c) E-W displacement of station P325

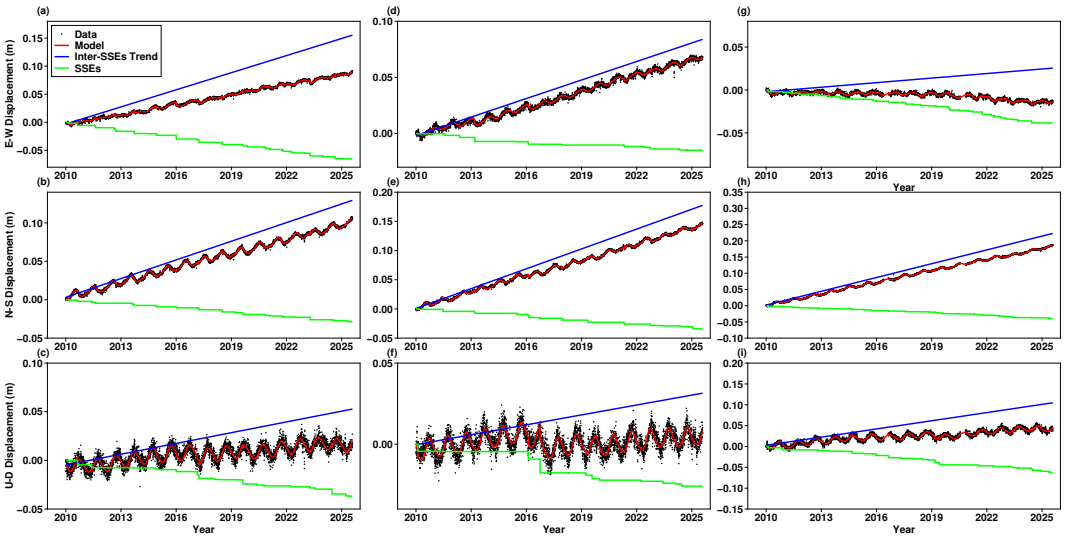

Figure S3. Example of the least-squares fit (Eq. S1) to the E-W, N-S, and U-D components of the stations ALBH, P375, and P325. Black dots show the displacement data while the red line shows the best-fit model, including the inter-SSEs secular velocity, SSEs steps, and seasonal contribution. The blue line shows the inter-SSEs secular motion contribution, and the green line shows the SSEs contribution to the time series. (a-c) are the E-W, N-S, and U-D components of station ALBH. (d-f) are the displacement time series of station P375. (g-i) are the displacement time series of station P325

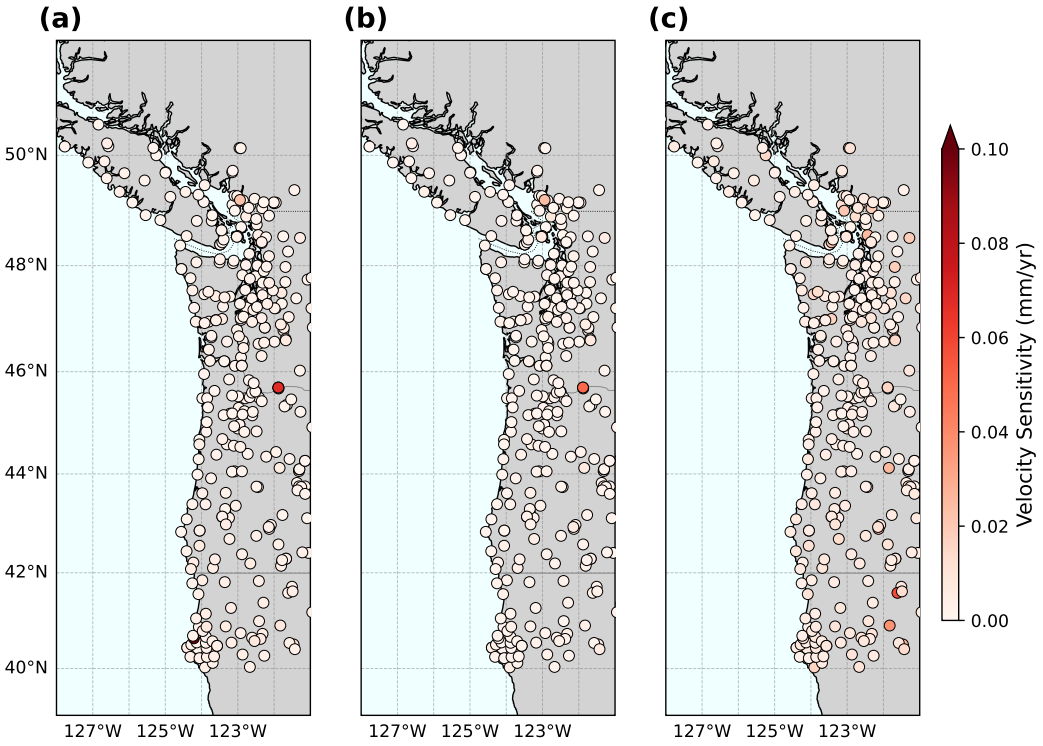

Figure S4. Sensitivity of Cascadia inter-SSE velocity field to ETS detection parameters. The maps show the variability of the derived secular velocity at each GNSS station, calculated as the range between the 95$^{\text{th}}$ and 5$^{\text{th}}$ percentiles across an ensemble of 530 parameter combinations (varying tremor radius, count threshold, and minimum duration). Panels (a), (b), and (c) correspond to the East-West, North-South, and Up-Down velocity components, respectively.

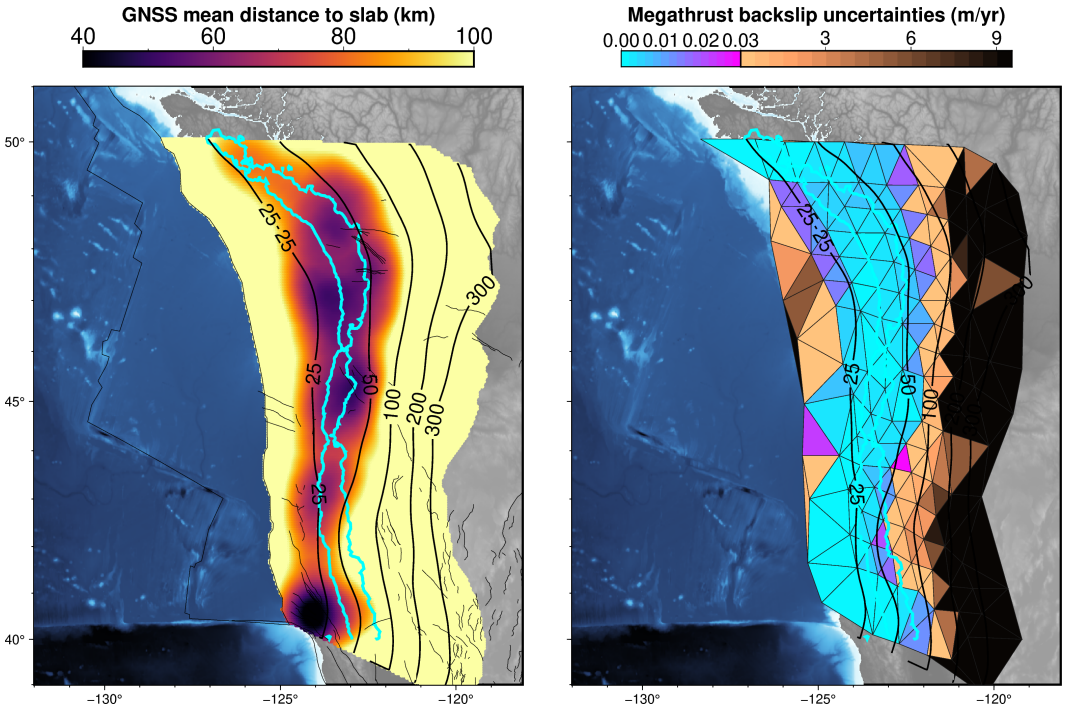

Figure S5. Coupling model resolution and uncertainties. (a) Mean distance of the Cascadia subduction slab from the onshore geodetic network. We define the mean distance as the average distance to the 20 closest GNSS stations for each point on the subdaction interface. Resolution of geodetic inversion diminishes rapidly at a rate $\sim \quad 1/r^2$ from the geodetic network. The ETS region of interest (cyan polygon) is the closest to the geodetic network along the subducting interface. (b) uncertainties of the coupling inverse model calculated as the diagonal of the model covariance matrix diag($\boldsymbol{C}_m$) for $\boldsymbol{C}_m \quad = \quad \left(\boldsymbol{A}^T \boldsymbol{C}_d \boldsymbol{A}\right)^{-1}$ where $\boldsymbol{C}_d$ is the diagonal matrix with the GNSS data uncertainties on its diagonal

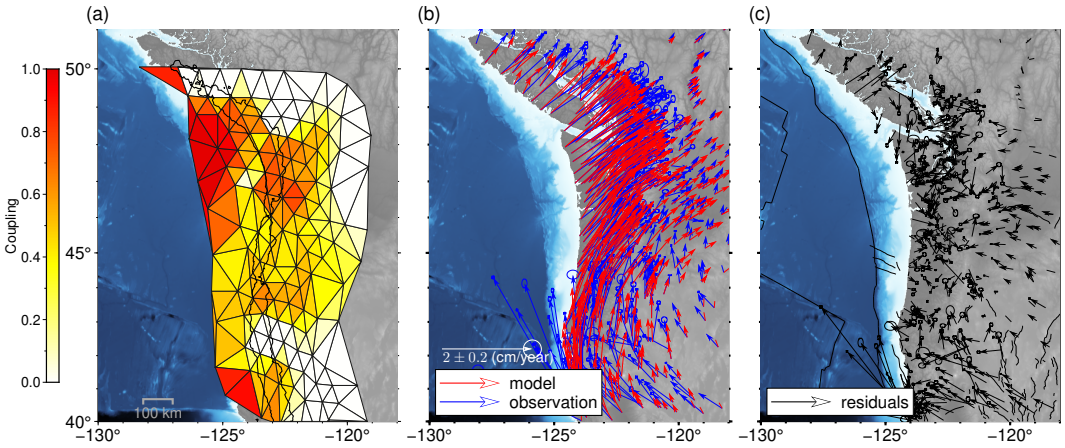

Figure S6. Inter-SSEs coupling model, and data fit. (a) Inter-SSEs coupling model, the black polygon shows the ETS region of interest. (b) GNSS network data and model displacements. (c) GNSS residuals

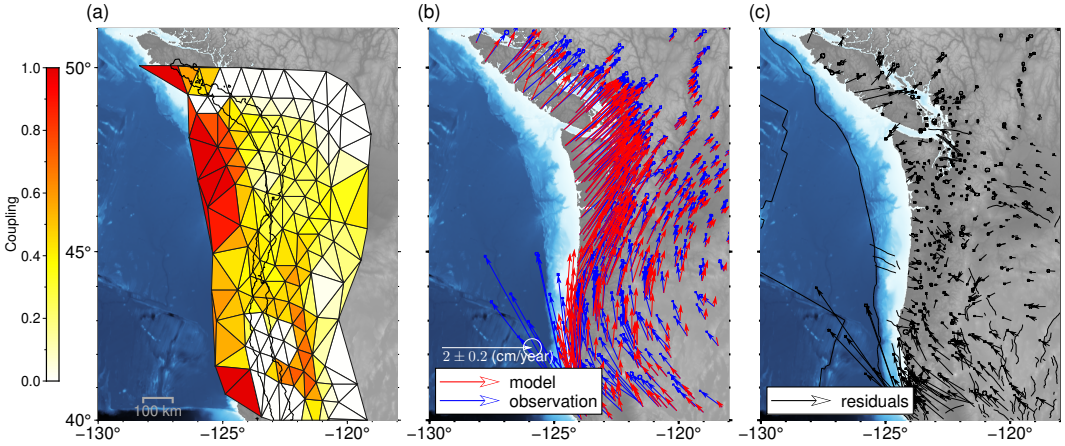

Figure S7. Inter-SSEs coupling model, and data fit. (a) long-term secular velocity (MIDAS Blewitt et al., 2018) coupling model, the black polygon shows the ETS region of interest. (b) GNSS network data and model displacements. (c) GNSS residuals

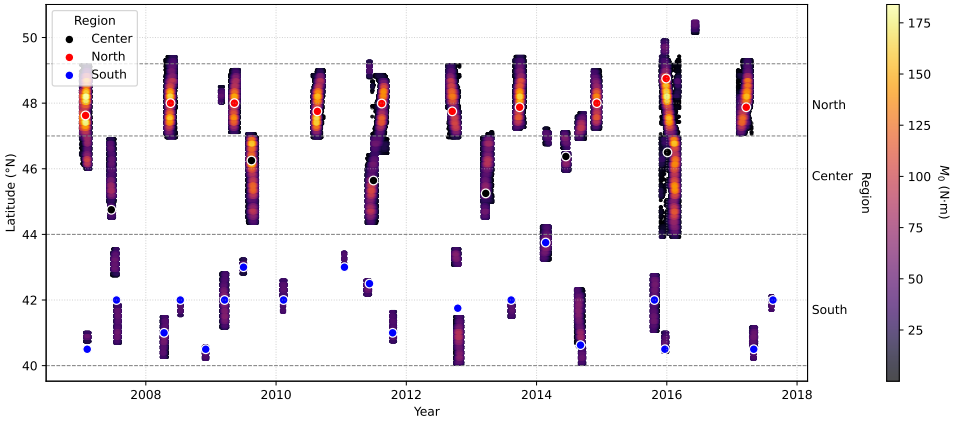

Figure S8. Extracting SSEs segments characteristics from the moment rate inversion data of Michel et al. (2019). Background color shows the SSEs moment rate, events within the same segment that are separated by an interval smaller than 2 months are sampled as one event.

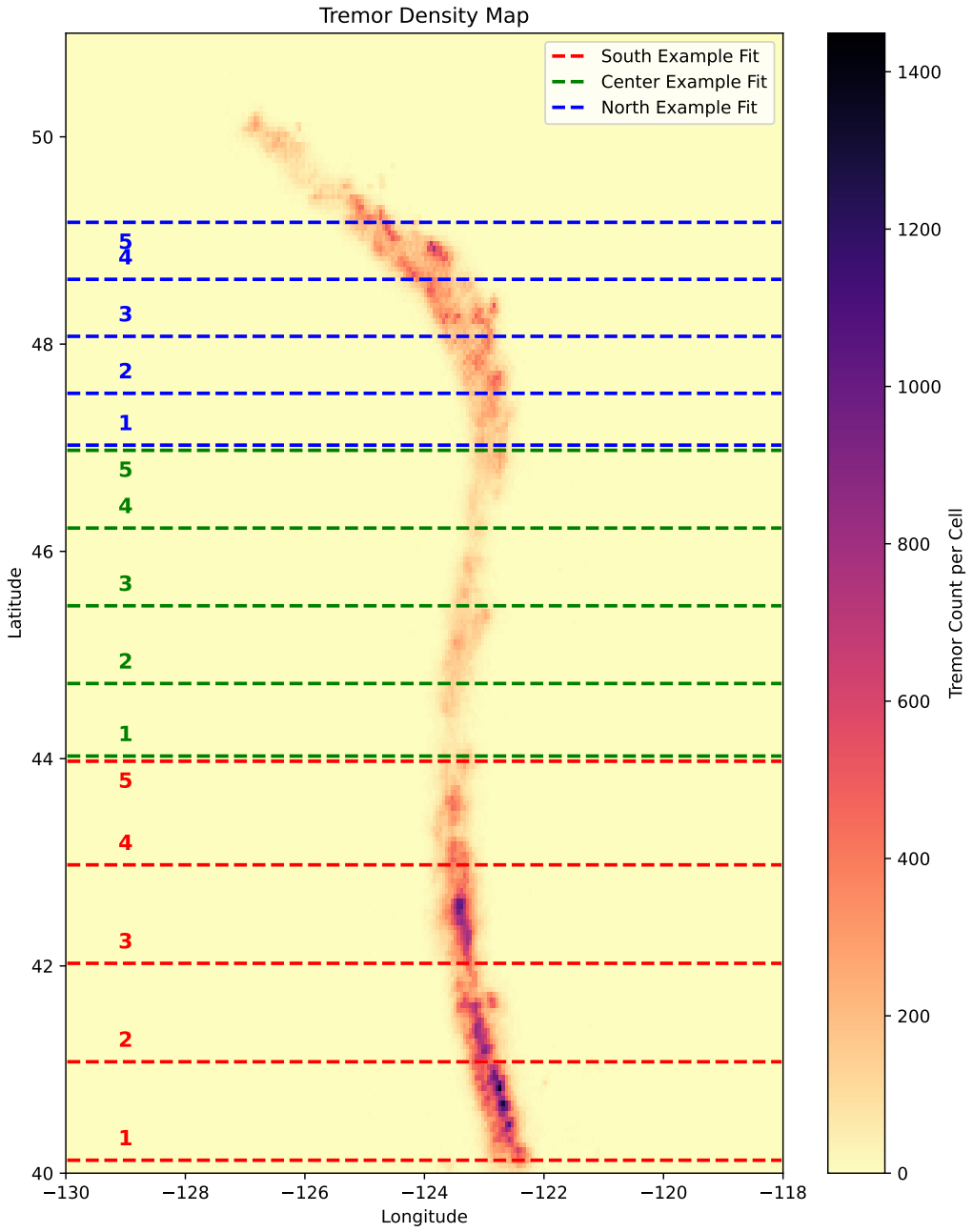

Figure S9. Cascadia tremor density map. number of tremors (Wech & Creager, 2008; Wech, 2010, 2021) in 0.05 × 0.05 cell grid along the Cascadia margin. Red, green, and blue lines show the location of 5 example profiles for each of the southern, central, and northern Cascadia segments presented in Figure S10.

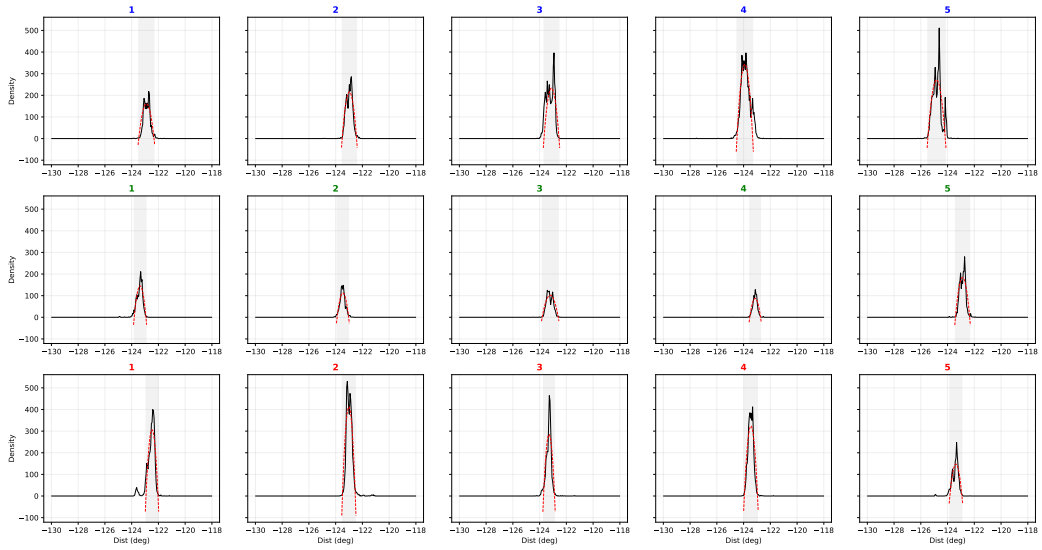

Figure S10. Tremor density profiles. (15) Longitudinal tremor density profile across the Cascadia margin. The black line shows the tremor density, while the red dashed line represents a second-order polynomial fit. The gray background indicates the width of the ETS region. The profile numbers and colors correspond to those in Figure S9.

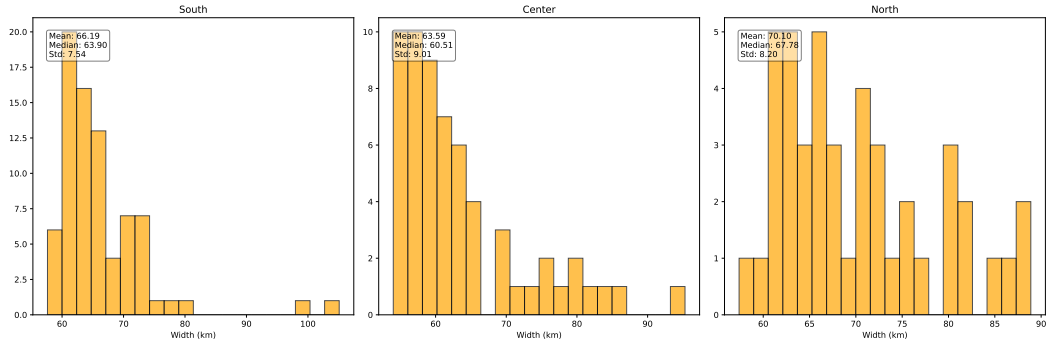

Figure S11. ETS zone width statistics. Histogram of the ETS width derived from latitudinal profiles (Figure S10), with widths projected onto the subduction interface. The analysis includes 78 profile widths for the South, 60 for the Center, and 44 for the North segments.